

An assessment of photometric redshift PDF performance in the context of LSST

S.J. Schmidt¹, A.I. Malz^{2,3}, J.Y.H. Soo⁴, M. Brescia⁵, S. Cavaudi^{5,6}, G. Longo⁶, I.A. Almosallam^{7,8}, M.L. Graham⁹, A.J. Connolly⁹, E. Nourbakhsh¹, J. Cohen-Tanugi¹⁰, H. Tranin¹⁰, P.E. Freeman¹¹, K. Iyer¹², J.B. Kalmbach¹³, E. Kovacs¹⁴, A.B. Lee¹¹, C. Morrison⁹, J. Newman¹⁵, E. Nuss¹⁰, T. Pospisil¹¹, M.J. Jarvis^{16,17}, R. Izbicki^{18,19}

(LSST Dark Energy Science Collaboration)

¹ Department of Physics, University of California, One Shields Ave., Davis, CA, 95616, USA

² Center for Cosmology and Particle Physics, New York University, 726 Broadway, New York, 10003, USA

³ Department of Physics, New York University, 726 Broadway, New York, 10003, USA

⁴ Department of Physics and Astronomy, University College London, Gower Street, London WC1E 6BT, UK

⁵ INAF-Capodimonte Observatory, Salita Moiariello 16, I-80131, Napoli, Italy

⁶ Department of Physics E. Pancini, University Federico II, via Cinthia 6, I-80126, Napoli, Italy

⁷ King Abdulaziz City for Science and Technology, Riyadh 11442, Saudi Arabia

⁸ Information Engineering, Parks Road, Oxford, OX1 3PJ, UK

⁹ Department of Astronomy, University of Washington, Box 351580, U.W., Seattle WA 98195, USA

¹⁰ Laboratoire Univers et Particules de Montpellier, Université de Montpellier, CNRS, Montpellier, France

¹¹ Department of Statistics & Data Science, Carnegie Mellon University, 5000 Forbes Avenue, Pittsburgh, PA 15213, USA

¹² Department of Physics and Astronomy, Rutgers, The State University of New Jersey, 136 Frelinghuysen Road, Piscataway, NJ 08854-8019 USA

¹³ Department of Physics, University of Washington, Box 351560, Seattle, WA 98195, USA

¹⁴ Argonne National Laboratory, Lemont, IL 60439, USA

¹⁵ Department of Physics and Astronomy and PITT PACC, University of Pittsburgh, 3941 O'Hara St., Pittsburgh, PA 15260, USA

¹⁶ Astrophysics, Department of Physics, University of Oxford, Denys Wilkinson Building, Keble Road, Oxford, OX1 3RH, UK

¹⁷ Department of Physics and Astronomy, University of the Western Cape, Bellville 7535, South Africa

¹⁸ Department of Statistics, Federal University of Sao Carlos, Sao Carlos, Brazil

¹⁹ External collaborator

12 October 2018

ABSTRACT

Photometric redshift (photo- z) probability distribution functions (PDFs) are a key data product of nearly all upcoming galaxy imaging surveys. However, the photo- z PDFs resulting from different techniques are not in general consistent with one another, and an optimal method for obtaining an accurate PDF remains unclear. We present the results of an initial study of the Large Synoptic Survey Telescope Dark Energy Science Collaboration (LSST-DESC), the first in a planned series of papers testing multiple photo- z codes on simulations of upcoming LSST galaxy photometry catalogues. This initial test evaluates photo- z algorithms in the presence of representative training data and in the absence of several common sources of systematic errors that affect the procedures by which photo- z PDFs are derived. The photo- z PDFs are evaluated using multiple metrics and we observe several trends, including an overall over/under-prediction in the broadness of the PDFs for several of the codes. A careful accounting of all systematics discovered will be necessary for the codes employed in upcoming analyses in order to achieve unbiased cosmological measurements.

Key words: galaxies: distances and redshifts – galaxies: statistics – methods: statistical

1 INTRODUCTION

² Large-scale photometric galaxy surveys are entering a new

³ era with currently or soon-to-be running Stage III and Stage

2 LSST Dark Energy Science Collaboration

IV dark energy experiments like the Dark Energy Survey (DES, Abbott et al. 2005), the Kilo-Degree Survey (KiDS, de Jong et al. 2013), Hyper Suprime-Cam (HSC) Survey (Aihara et al. 2018a,b), Large Synoptic Survey Telescope (LSST, Abell et al. 2009), Euclid (Laureijs et al. 2011), and Wide-Field Infrared Survey Telescope (WFIRST, Green et al. 2012). The move to imaging based surveys, rather than spectroscopic based, for cosmological measurements makes proper understanding of photometric redshifts (“photo- z ’s”) of paramount importance, as cosmological distance measures for statistical samples are directly dependent on photo- z measurements.

The unprecedented sample size of LSST galaxies, expected to number several billion for the main cosmological sample, necessitates stringent constraints on photo- z accuracy if systematic errors are not to dominate the statistical errors. The LSST Science Requirements Document (SRD)¹ lists the photometric redshift goals for a magnitude limited sample with $i < 25$ as: root-mean-square error with a goal of $\sigma_z < 0.02(1+z)$; 3σ “catastrophic outlier” rate below 10%; bias below 0.003². The LSST Dark Energy Science Collaboration (LSST-DESC) developed a separate Science Requirements Document (The LSST Dark Energy Science Collaboration et al. 2018), which forecasts the constraining power of five cosmological probes using somewhat conservative assumptions to define requirements on systematic errors for several measurements. These include even more stringent requirements on photometric redshift performance than those included in the LSST SRD, though the initial LSST-DESC requirements are defined for tomographic bin populations. The tremendous size of LSST’s galaxy catalogue will be enabled by its exceptional depth, pushing to fainter magnitudes and deeper imaging and including galaxies of lower luminosity and higher redshift than ever before. The inclusion of these populations introduce major physical degeneracies, for example the Lyman break/Balmer break degeneracy, that were not present in the populations covered in shallower large area surveys like the Sloan Digital Sky Survey (SDSS, York et al. 2000) and the Two Micron All Sky Survey (2MASS, Skrutskie et al. 2006). These issues are not unique to LSST, and are present in Stage III Dark Energy surveys; however, in order to meet the demanding error budgets of Stage IV projects such as LSST and LSST-DESC it will be necessary to fully characterize those degeneracies wherein multiple redshift solutions have comparable likelihood to per cent level accuracy.

There is often a desire to have a single valued “point-estimate” redshift for an individual galaxy. However, the complex, non-linear (and often non-unique) nature of the mapping between broad band fluxes and redshift means that a single value is unable to capture the full redshift information encoded in a galaxy’s magnitudes. For example, a common point-estimate for a template-based method is taking the highest likelihood solution as the point photo- z . A single valued redshift ignores degenerate redshift solutions

of lower probability, potentially biasing photometric redshift estimates both for individual galaxies and ensemble distributions. Storing more information is necessary, most often photo- z codes output the redshift probability density function, also often referred to as $p(z)$, describing the relative likelihood as a function of redshift. Early template methods such as Fernández-Soto et al. (1999) converted relative χ^2 values of template spectra to likelihoods to estimate $p(z)$. Soon after, codes such as Benítez (2000) added a Bayesian prior and output a posterior probability distribution. While many early machine learning based algorithms focused on a point-estimate, Firth et al. (2003) used a neural net with 1000 realizations scattered within the photometric errors to estimate a $p(z)$. As more groups began to employ photometric redshifts in their cosmological analyses, there was a realization that point-estimate photo- z ’s were inadequate for precision cosmology measurements (Mandelbaum et al. 2008). From around this point onward, most photo- z algorithms have attempted to implement some estimate of the overall redshift probability in their outputs, and some surveys began supplying a full $p(z)$ rather than a simple redshift point-estimate and error (e. g. de Jong et al. 2017).

For cosmological measurements, certain science cases require redshift information on individual objects, e. g. identification of host galaxy redshift for supernova classification, or identifying potential cluster membership. Other science cases seem to need only ensemble redshift information; for instance many current cosmic shear techniques require only the overall redshift distribution $N(z)$ for tomographic redshift samples. However, recent data-driven techniques employing hierarchical Bayesian or Gaussian Process methods have emerged that calibrate redshift distributions using individual $p(z)$ estimates (e. g. Sánchez & Bernstein 2018). These methods assume that the $p(z)$ for each galaxy is an accurate PDF, and such methods break down if this assumption is invalid. Thus, even methods that seem to need only ensemble $N(z)$ may actually require accurate $p(z)$ in order to meet stringent survey requirements. Large photometric surveys such as LSST must develop algorithms that simultaneously meet the needs of all science cases. In order to meet these ambitious goals for photo- z accuracy, every aspect of photo- z estimation will have to be optimized: the algorithms employed, both template and machine-learning based (both in design and implementation); the spectroscopic data used as a training set for machine learning algorithms or to estimate template sets and train Bayesian priors; and probabilistic catalogue compression schemes that balance information retention against limited storage resources.

There are numerous techniques for deriving photo- z PDFs from photometry, yet no one method has yet been established as clearly superior. Quantitative comparisons of photo- z methods have been made before. The Photo- z Accuracy And Testing (PHAT, Hildebrandt et al. 2010) effort focused on point estimates derived from many photometric bands. Rau et al. (2015) introduced a new method for improving redshift PDFs using an ordinal classification algorithm. DES compared several codes for point estimates (Sánchez et al. 2014) and a summary statistic of photo- z interim posteriors for tomographically binned galaxy subsamples (Bonnett et al. 2016). This paper is distinguished by its focus on metrics of photo- z interim posteriors themselves and consideration of both classic and state-of-the-art

¹ available at <https://docushare.lsstcorp.org/docushare/dsweb/Get/LPM-17>

² Note that at the time the SRD was written, these goals were stated in terms of a photo- z point estimate for each galaxy, as was standard in many previous studies, while in this paper we emphasize the importance of using a full photo- z PDF.

photo- z algorithms, comparing the performance of several of the most widely employed codes as well as some that have been developed only recently on the basis of metrics appropriate for a probabilistic data product. The results presented in this work are a major focus of the Photometric Redshift working group of the LSST-DESC. This work is laid out in the Science Roadmap (SRM)³ as one of the critical activities to be completed in preparation for dark energy science analysis on the first year LSST data. This is the first of multiple papers by the working group, which will grow in sophistication. In this initial paper we focus on evaluating the performance of photometric redshift codes and PDF-based performance metrics in the presence of representative training sets. Comparing the relative performance of the codes enables us to evaluate whether each code is using information in an optimal way, and may reveal enhancements in some codes and deficiencies in others, either in the fundamental algorithm, or in specific implementation. We note that these initial tests are a necessary requirement for photo- z codes that will be used in cosmological analyses; however, meeting these requirements is only the first stage in the process of accounting for incomplete training samples, object blending, the robustness of estimated redshift distributions when combining redshift estimates in tomographic bins, and other complications that realistic samples will encounter in estimating photometric redshifts. This can be thought of as an initial test under near perfect conditions before further complexities are added in future papers.

Before moving forward, we must address how the best methods may be unique to the performance metrics and science cases considered and what distinguishes photo- z PDFs of different methods from one another. Though photo- z PDFs are often written simply as $p(z)$, the PDF itself must be an interim posterior distribution $p(z|d, I)$, the probability of redshift conditioned on photometric data d that has actually been observed and the prior information I that guides how a redshift is extracted from the photometry. If we run multiple photo- z codes on a single dataset, the photo- z interim posteriors will not be identical because each code is based on assumptions in the form of an interim prior — these assumptions form the premise for photo- z estimation as a whole and are the only way to introduce differences in estimates of what would otherwise be a shared photo- z posterior $p(z|d)$ regardless of the code used to obtain it. Though explicit knowledge of the interim prior is necessary to use photo- z interim posteriors self-consistently in physical inference, the interim prior of a particular methodology is often implicit and not necessarily shared among all galaxies in the catalogue.

This paper therefore aims (1) to constrain the impact of the interim prior I by separating it into a component I_H representing the method itself and a component I_D representing physical information, such as a training set or SED template library and (2) to present a procedure for evaluating the performance of photo- z codes in generic tests that may include many more systematics in the interim prior I . In order to isolate the effects encapsulated by I_H of variation between codes from issues with the training set or template library

encapsulated by I_D , we use an identical set of simulated galaxies for every code and construct a template library and training sample that are *complete and representative* and shared among all codes; that is, our training sample for machine learning codes is drawn from the same underlying galaxy population as our test set, with no additional selections, and the SED library used for template-based codes is the same as the one used to generate the photometric data. We explore a number of performance metrics in this paper, not to make a conclusion regarding the superiority or even relative favorability of each code but to establish a method for comparing photo- z PDFs derived by different methods. These test conditions set the stage for addressing in a future paper the crucial issue of incomplete and non-representative prior information.

The outline of the paper is as follows: in § 2 we present the simulated data set; in § 3 we describe the current generation codes employed in the paper; in § 4 we discuss the interpretation of photo- z PDFs in terms of metrics of accuracy; in § 5 we show our results and compare the performance of the codes; in § 6 we offer our conclusions and discuss future extensions of this work.

2 THE SIMULATION AND MOCK GALAXY CATALOG

In order to test the current generation codes, we employ a simulated galaxy catalogue. The simulation is completely catalogue-based, with no image construction or mock measurements made. We describe these in detail below.

2.1 Buzzard-v1.0 simulation

The BUZZARD-HIGHRES-V1.0 put in cites to in prep Buzzard papers catalogue construction started with a dark matter only simulation. This N-body simulation contained 2048³ particles in a 400 Mpc h⁻¹ box. [N] snapshots (with smoothing and interpolation between snapshots) were saved in order to construct a lightcone. Dark matter halos were identified using the ROCKSTAR software package (Behroozi et al. 2013). These dark matter halos were populated with galaxies with a stellar mass and absolute r -band magnitude in the SDSS system determined using a sub-halo abundance matching model constrained to match both projected two-point galaxy clustering statistics and an observed conditional stellar mass function (Reddick et al. 2013).

To assign an SED to each galaxy, the *Adding Density Dependent Spectral Energy Distributions* (ADDSEDS, deRose in prep.)⁴ procedure was used. This consisted of training an empirical relation between absolute r -band magnitude, local galaxy density, and SED using a sample of $\sim 5e^5$ galaxies from the magnitude-limited Sloan Digital Sky Survey Data Release 6 Value Added Galaxy Catalog (Blanton et al. 2005)[Note: is this the proper reference to SDSS-NYU VAGC? File is called combined_dr6_cooper.fits, but I don't see which Cooper et al 2006 this is supposed to refer to?]. Each SDSS spectrum is fit with a sum of five

³ Available at: http://lsst-desc.org/sites/default/files/DESC_SRML_V1_1.pdf

⁴ <https://github.com/vipasu/addseds>

4 LSST Dark Energy Science Collaboration

232 SED components using the K-CORRECT v? software pack-
233 age⁵ (Blanton & Roweis 2007), thus each galaxy SED is pa-
234 rameterized as five weights for the basis SEDs. The distance
235 to the spatial projected fifth-nearest neighbour was used as a
236 proxy for local density in the SDSS training sample. For each
237 simulated galaxy, a “random” [details] galaxy with “similar”
238 [details] absolute r -band magnitude and local galaxy density
239 was chosen from the training set, and that training galaxy’s
240 SED was assigned to the simulated galaxy. Given the SED,
241 absolute r -band magnitude and redshift, we computed ap-
242 parent magnitudes in the six LSST filter passbands, $ugrizy$.
243 We assigned magnitude errors in the six bands using the
244 simple model described in Ivezić et al. (2008), assuming full
245 10-year depth observations had been completed. The num-
246 ber of total 30-second visits assumed when generating the
247 photometric errors differs slightly from the fiducial numbers
248 assumed for LSST: we assume 60 visits in u-band, 80 vis-
249 its in g-band, 180 visits in r-band, 180 visits in i-band, 160
250 visits in z-band, and 160 visits in y-band.

251 2.1.1 Selection of training and test sets

252 The total catalogue covered 400 square degrees and con-
253 tained 238 million galaxies to an apparent magnitude limit
254 of $r = 29$ and spanning the redshift range $0 < z \leq 8.7$. This
255 catalogue contained two orders of magnitude more galaxies
256 than were needed for this study, so only ~ 8 square degrees
257 were used. Systematic problems with galaxy colors above
258 $z > 2$ were observed, so the catalogue was trimmed to in-
259 clude only galaxies in the redshift range $0 < z \leq 2.0$. A
260 random subset of the the remaining galaxies was chosen,
261 and placed at random into either a “training” set (10 per
262 cent of the sample), for which the galaxies true redshifts
263 will be supplied, or a “test” set (the remaining 90 per cent
264 of the sample), for which each code will need to predict a
265 redshift PDF for each galaxy. The resulting catalogues con-
266 tain 111 171 training galaxies and 1 000 883 test galaxies. We
267 restrict our analysis to a sample with $i < 25.3$, which give a
268 signal-to-noise ~ 30 for most galaxies, a cut often referred
269 to as the expected “LSST Gold Sample”. This magnitude
270 cut results in a training set with 44 404 galaxies and a test
271 set containing 399 356 galaxies. All subsequent results will
272 evaluate this “gold sample” test set.

273 2.1.2 Templates

274 As mentioned in Section 2.1, the SEDs in the Buzzard sim-
275 ulation are drawn from an empirical set of SEDs taken from
276 the SDSS DR6 NYU-VAGC, a sample of roughly $\sim 5e^5$
277 galaxies with spectra in SDSS. To determine a finite set of
278 templates to use with template fitting codes we take the five
279 SED weight coefficients for each of the $\sim 500\,000$ galaxies in
280 the SDSS sample and run a simple K-means clustering algo-
281 rithm on this five dimensional space. The K-means cluster
282 centres span the space of coefficients and properly reflect the
283 underlying density in the coefficient space, thus providing a
284 reasonable approximation for a spanning SED set. An ad-
285 hoc number of $K = 100$ was chosen and the 100 K-means
286 centre positions are taken as the weights for the K-CORRECT

287 SED components to construct one hundred template SEDs.
288 These 100 templates were provided, however not every tem-
289 plate code uses this set of one hundred templates: because
290 EAZY was designed and written to use the same five basis
291 templates employed by K-CORRECT when constructing our
292 mock galaxies, EAZY was run using linear combinations of
293 these five templates rather than using the 100 discrete tem-
294 plates.

295 2.1.3 Limitations

296 For our initial investigation of photometric redshift codes,
297 we begin with a data set that is somewhat idealized, and
298 does not contain all of the complicating factors present in
299 real data. In several cases, the simplification is done with
300 a purpose, with potentially confounding effects excluded
301 in order to better isolate the differences between current-
302 generation photo-z codes, and their causes. We list several
303 of the simulations limitations in this section. As the sim-
304 ulation is catalogue-based, no image level effects, such as
305 photometric measurement effects, object blending, contami-
306 nation from sky background (Zodiacal light, scattered light,
307 etc...), lensing magnification, or Galactic reddening are in-
308 cluded. No stars are included in the catalogue, nor are the
309 effects of AGN. As all SEDs are constructed from only five
310 basis templates, properties of the galaxy population will be
311 restricted to follow linear combinations of the characteristics
312 of the five basis templates, so certain non-linear features, for
313 example the full range of emission line fluxes relative to the
314 continuum, will not be included in the model galaxy pop-
315 ulation. No additional dust reddening intrinsic to the host
316 galaxy is included, the only approximation of dust extinc-
317 tion comes in the form of dust encoded in the five basis SEDs
318 via the training set used to create the basis templates. Sim-
319 ple linear combinations of these basis templates will, once
320 again, not explore the full range of realistic dust extinction
321 observed in galaxy populations.

3 METHODS

322 Here we outline the photo-z PDF codes tested in this study.
323 In total, eleven distinct codes are tested. This sample is not
324 comprehensive, but does cover a broad range of current-
325 generation codes. Both template-based and machine learn-
326 ing approaches are included and each are described sepa-
327 rately in Secs. 3.1 and 3.2 respectively. The list of codes are
328 summarized in Table 1.

329 The questions that must be answered for each code are:
330 what unique features are included in the specific implemen-
331 tation that influence the output $p(z)$. What form of vali-
332 dation was performed with the training data, how were pho-
333 tomatic uncertainties employed in the analysis, how were
334 negative fluxes treated, what specific prior form was em-
335 ployed (for template based codes), or what specific machine
336 learning architecture was used (for ML codes)?

⁵ <http://kcorrect.org>

Table 1. List of photo- z codes featured in this study. ML here means machine learning.

Code	Type	Paper	Website
BPZ	template	Benítez (2000)	http://www.stsci.edu/~dcoe/BPZ/
EAZY	template	Brammer et al. (2008)	https://github.com/gbrammer/eazy-photoz
LePHARE	template	Arnouts et al. (1999)	http://www.cfht.hawaii.edu/~arnouts/lephare.html
ANNz2	ML	Sadeh et al. (2016)	https://github.com/IftachSadeh/ANNz2
DELIGHT	ML/template	Leistedt & Hogg (2017)	https://github.com/ixxael/Delight
FLEXZBOOST	ML	Izbicki & Lee (2017)	https://github.com/tospisic/flexcode; https://github.com/rizbicki/FlexCoDE
GPz	ML	Almosallam et al. (2016b)	https://github.com/OxfordML/GPz
METAPhOR	ML	Cavuoti et al. (2017a)	http://dame.dsfa.unina.it
CMNN	ML	Graham et al. (2018)	-
SKYNET	ML	Graff et al. (2014)	http://ccpforge.cse.rl.ac.uk/gf/project/skynet/
TPZ	ML	Carrasco Kind & Brunner (2013)	https://github.com/mgckind/MLZ
TRAINZ	N/A	See Section 3.3	

3.1 Template-based Approaches

3.1.1 BPZ

BPZ⁶ (Bayesian Photometric Redshift, Benítez 2000) is a template-based photo- z code that compares the expected colors (C) calculated for a set of spectral energy distribution (SED) types/templates (T) to the observed colors to calculate the likelihood of observing colors at each redshift for each type, $p(C|z, T)$. The code employs an empirically determined Bayesian prior in apparent magnitude (m_0) and SED-type. Assuming that the SED-types are spanning and exclusive, we can determine the redshift posterior $p(z|C, m_0)$ by marginalizing over all SED-types with a simple sum (Eq. 3 from Benítez 2000):

$$p(z|C, m_0) \propto \sum_T p(z, T|m_0) p(C|z, T) \quad (1)$$

where the first term on the right-hand side is the Bayesian prior and the second term is the traditional likelihood. The prior is assumed to have the form: $p(z, T|m_0) = p(T|m_0) p(z|T, m_0)$, i.e. it parameterizes the prior as an evolving type fraction with apparent magnitude, combined with a prior on the expected redshift probability distribution as a function of both apparent magnitude and SED-type.

In this paper we use BPZ v 1.99.3. The template set employed here is the set of 100 discrete SEDs described in Section 2.1.2 To keep the number of free parameters to a manageable level the SEDs in the training set are sorted by the rest-frame $u-g$ colour and split into three “broad” SED classes, equivalent to the E, Sp and Im/SB types in Benítez (2000). We assume the same functional form for the Bayesian priors as used by Benítez (2000), and utilize the training-set galaxies with known SED-type, redshift, and apparent magnitude to determine the type fractions and the best fit for the eleven free parameters of the prior. For galaxies with negative flux in a measured band, the placeholder value is replaced with an estimate one σ detection limit in that particular band, i. e. a value close to the estimated sky noise threshold. The type-marginalized $p(z)$ is generated by setting the parameter PROBS_LITE=TRUE in the BPZ parameter file.

⁶ <http://www.stsci.edu/~dcoe/BPZ/>

3.1.2 EAZY

EAZY⁷ (Easy and Accurate Photometric Redshifts from Yale, Brammer et al. 2008) is a template-based photo- z code that includes several features that improve on the basic χ^2 fit used in many template codes. It can fit the observed photometry with SEDs created from a linear combination of a set of templates at each redshift, and the best-fit SED is found by simultaneously fitting one, two or all of the templates by minimizing χ^2 . The minimized $\chi^2(z)$ is then combined with an apparent magnitude prior to obtain the posterior redshift probability distribution, although some argue that this is not the mathematically correct way of calculating the posteriors. EAZY can also account for the uncertainties in the templates by adding an empirically derived template error in quadrature as a function of redshift to the flux errors.

In this paper we use the all-templates mode, which fits the photometric data with a linear combination of the five basis templates. We employed the 5 basis templates described in Section 2.1, and set the template error to zero since these same templates were used to produce the simulated catalog photometry. The likelihoods are calculated on a 200-point redshift grid spanning $0 \leq z \leq 2$, and include the application of a type-independent apparent magnitude prior estimated from the training data.

3.1.3 LePhare

LEPHARE⁸ (Photometric Analysis for Redshift Estimate, Arnouts et al. 1999; Ilbert et al. 2006) is a photo- z reconstruction code based on a χ^2 template-fitting procedure. The observed colors are matched with the colours predicted from a set of spectral energy distribution (SED) which can be either synthetic or based on a semi-empirical approach. LEPHARE has been used to produce the COSMOS2015 photo- z catalogue (Laigle et al. 2016).

Each SED is redshifted in steps of $\Delta z = 0.01$ and convolved with the simulated LSST filter transmission curves (accounting for instrument efficiency). The opacity of the inter-galactic medium has been set to zero as no additional

⁷ <https://github.com/gbrammer/eazy-photoz>

⁸ <http://www.cfht.hawaii.edu/~arnouts/lephare.html>

6 LSST Dark Energy Science Collaboration

413 reddening has been included in the Buzzard simulations.
 414 The computed photo- z is then the value that minimizes the
 415 merit function $\chi^2(z, T, A)$ from Arnouts et al. (1999):

$$416 \quad \chi^2(z, T, A) = \sum_f^{N_f} \left(\frac{F_{\text{obs}}^f A \times F_{\text{pred}}^f(T, z)}{\sigma_{\text{obs}}^f} \right)^2 \quad (2)$$

417 where A is a normalization factor, $F_{\text{pred}}^f(T, z)$ is the flux
 418 predicted for a template T at redshift z . F_{obs}^f is the observed
 419 flux in a given band f and σ_{obs}^f the associated observational
 420 error. The index f refers to the considered band and N_f is
 421 the total number of filters.

422 In this paper we use LEPHARE v 2.2. The set of tem-
 423 plates used for fitting the photo- z 's are the 100 discrete Buzz-
 424 ard SED templates as described in section 2.1.2. The full
 425 $p(z)$ corresponds to the likelihoods calculated at each point
 426 on our z -grid.

427 3.2 Training-based Codes

428 3.2.1 ANNz2

429 ANNz2⁹ (Sadeh et al. 2016) is a powerful package that
 430 has the ability to employ several machine learning algo-
 431 rithms, including artificial neural networks (ANN), boosted
 432 decision tree (BDT) and k-nearest neighbour (KNN). Us-
 433 ing the Toolkit for Multivariate Data Analysis (TMVA)
 434 with ROOT¹⁰, it can run multiple machine learning algo-
 435 rithms for a single training and outputs photo- z 's based on
 436 a weighted average of their performances.

437 ANNz2 is capable of producing both photo- z point es-
 438 timates and redshift posterior probability distributions $p(z)$,
 439 it could also conduct classifications and supports reweight-
 440 ing between samples. The PDFs are produced by propa-
 441 gating the intrinsic uncertainty on the input parameters
 442 and the uncertainty in the machine learning method to
 443 the expected photo- z solution, averaged over multiple runs
 444 weighted based on the performance of each run. ANNz2
 445 presents its photo- z uncertainty different from many codes
 446 by using the KNN method: it estimates the photo- z bias be-
 447 tween each object and a fixed number of nearest neighbours
 448 in parameter space, it then takes the 68th percentile width of
 449 the distribution of the bias. This is based on the implication
 450 that objects with similar photometric properties would have
 451 similar uncertainties, and therefore the photometric errors
 452 of the inputs are not propagated into the code.

453 In this study, ANNz2 v. 2.0.4 was used. The full PDF
 454 for each galaxy is also produced with a linear stepsize of
 455 $z = 0.01$ for $0 \leq z \leq 2$. A set of 5 ANNs with architec-
 456 ture 6 : 12 : 12 : 1 (6 *ugrizy* inputs, 2 hidden layers with
 457 12 nodes each, and 1 output) with different random seeds
 458 are used during each training. Half of the training set is
 459 used as a validation set to prevent overtraining. All training
 460 objects are set to have detected magnitudes, however the
 461 non-detections ($\text{mag} = -99$) in the testing set are replaced
 462 with the mean of that particular band.

⁹ <https://github.com/IftachSadeh/ANNZ>

¹⁰ <http://tmva.sourceforge.net/>

463 3.2.2 Color-Matched Nearest-Neighbours

464 The nearest-neighbours color-matching photometric redshift
 465 estimator (CMNN) is presented in (Graham et al. 2018, her-
 466 after G18). This method uses a training set of galaxies with
 467 known redshifts that has equivalent or better photometry as
 468 the test set in terms of quality and filter coverage. For each
 469 galaxy in the test set we identify a color-matched subset of
 470 training galaxies, choose one (e.g. the nearest-neighbour or a
 471 random selection), and use its known redshift as the photo- z .
 472 This color-matched subset is identified by first calculating
 473 the Mahalanobis distance D_M in color-space between the
 474 test galaxy and all training-set galaxies: the difference be-
 475 between the test and a training set galaxy's color divided by
 476 the photometric error, summed over all colors (i.e., $u-g$, $g-r$,
 477 $r-i$, $i-z$, and $z-y$). Then, the threshold value for D_M that
 478 define a good color match is set by the percent point func-
 479 tion (PPF): for example, for $N_{\text{dof}} = 5$, PPF = 95 per cent
 480 of all training galaxies consistent with the test galaxy will
 481 have $D_M < 11.07$ (where N_{dof} , the number of degrees of
 482 freedom, is the number of colors). For a given test galaxy,
 483 the $p(z)$ is the normalized distribution of the true catalogue
 484 redshifts of this color-matched subset of training galaxies,
 485 and the standard deviation of the color-matched subset is
 486 used as the photo- z uncertainty.

487 We have applied the nearest-neighbours color-matching
 488 photometric redshift estimator described in G18 to the sim-
 489 uled data. Compared to its application in G18, there are
 490 some minor differences in the application of this estimator
 491 to the Buzzard catalogue. First, we do not impose non-
 492 detections on galaxies with a magnitude fainter than the ex-
 493 pected LSST 10-year limiting magnitude or bright enough to
 494 saturate with LSST: *all* of the photometry for all the galax-
 495 ies in the test and training sets are used for this experiment.
 496 Second, as in G18 we do apply an initial cut in color to
 497 the training set before calculating the Mahalanobis distance
 498 in order to accelerate processing, and also use a magnitude
 499 pseudo-prior to improve photo- z estimates, but for both we
 500 have used different cut-off values that are appropriate for the
 501 Buzzard galaxies' colors and magnitudes. Third, we set dif-
 502 ferent parameters for the identification of the color-matched
 503 subset of training galaxies and the selection of a photometric
 504 redshift estimate. In G18 we used a percent point function
 505 (PPF) value of 0.68 to identify the color-matched subset of
 506 training galaxies and used the redshift of nearest neighbour
 507 in color-space as the photo- z estimate. These choices work
 508 well when the desire is to obtain accurate photo- z estimates
 509 for most test-set galaxies, but does not return a robust $p(z)$
 510 in all cases – especially for galaxies that are bright and/or
 511 have few matches in color-space. Since a robust estimate
 512 of $p(z)$ is desired for this work we make several changes to
 513 our implementation of the CMNN photo- z estimator. We
 514 continue to use a percent point function of PPF = 0.95 to
 515 generate the subset of color-matched training galaxies, but
 516 weight them by the inverse of their Mahalanobis distance.
 517 This weighting maintains some of the accuracy that was pre-
 518 viously achieved by simply using the nearest neighbour in
 519 color-space. We then use the weights to create the $p(z)$ in-
 520 stead of having the redshift of each color-matched training-
 521 set galaxy count equally. To obtain a robust estimate of the
 522 $p(z)$ for galaxies with a small number of color-matched train-
 523 ing set galaxies, when this number is less than 20 the nearest

524 20 neighbours in color-space are used instead, and we con-
 525 volve the $p(z)$ with a Gaussian with a standard deviation
 526 of:

$$527 \quad \sigma = \sigma_{\text{train}} \sqrt{(\text{PPF}_{20}/0.95)^2 - 1} \quad (3)$$

528 to appropriately broaden it so that the $p(z)$ for these test
 529 galaxies represents the enlarged PPF value associated with
 530 it. Overall, these three changes will yield poorer accuracy
 531 photo- z compared to those presented in G18, but they will
 532 all have significantly more robust estimates of the $p(z)$, par-
 533 ticularly for the brightest test galaxies. This is sufficient
 534 for this work because, as described in G18, the goal of the
 535 CMNN photo- z estimator was never to provide the “best”
 536 (or even competitive) estimates in the first place, given its
 537 reliance on a deep training set, but rather to provide a means
 538 for direct comparisons between LSST photometric quality
 539 and photo- z estimates. With this work we show how the in-
 540 put parameters should be set in order to return robust $p(z)$
 541 estimates in addition to point value estimates.

542 3.2.3 Delight

543 DELIGHT¹¹ (Leistedt & Hogg 2017) infers photo- z ’s by using
 544 a data-driven model of latent SEDs and a physical model
 545 of photometric fluxes as a function of redshift. Generally,
 546 machine learning methods rely on representative training
 547 data with similar band passes, while template based meth-
 548 ods rely on a complete library of templates based on phys-
 549 ical models constructed. DELIGHT is constructed in attempt
 550 to combine the advantages and eliminate the disadvantages
 551 of both template-based and machine learning algorithms: it
 552 constructs a large collection of latent SED templates (or
 553 physical flux-redshift models) from training data, with a
 554 template SED library as a guide to the learning of the model.
 555 The advantage of DELIGHT is that it neither needs represen-
 556 tative training data in the same photometric bands, nor does
 557 it need detailed galaxy SED models to work.

558 This conceptually novel approach is done by using
 559 Gaussian processes operating in flux-redshift space. The pos-
 560 terior distribution on the redshift of a target galaxy is ob-
 561 tained via a pairwise comparison with training galaxies,

$$562 \quad p(z|\hat{\mathbf{F}}) \approx \sum_i p(\hat{\mathbf{F}}|z, t_i) p(z|t_i) p(t_i), \quad (4)$$

563 where $p(z|t_i)p(t_i)$ captures prior information about the red-
 564 shift distributions and abundances of the galaxies, with t_i
 565 denoting the galaxy template; while $p(\hat{\mathbf{F}}|z, t_i)$ is the poste-
 566 rior of noisy flux $\hat{\mathbf{F}}$ at redshift z . For each training-target
 567 pair, $p(\hat{\mathbf{F}}|z, t_i)$ is evaluated as follows:

$$568 \quad p(\hat{\mathbf{F}}|z, t_i) = \int p(\hat{\mathbf{F}}|\mathbf{F}) p(\mathbf{F}|z, z_i, \hat{\mathbf{F}}_i) d\mathbf{F}, \quad (5)$$

569 where $p(\hat{\mathbf{F}}|\mathbf{F})$ is the likelihood function, it compares the
 570 noisy real flux $\hat{\mathbf{F}}$ with the noiseless flux \mathbf{F} obtained from the
 571 linear combination of template models, carefully constructed
 572 to account for model uncertainties and different normaliza-
 573 tion of the same SED; while $p(\mathbf{F}|z, z_i, \hat{\mathbf{F}}_i)$ is the prediction

574 of flux at a different redshift z with respect to the training
 575 object with redshift z_i and flux $\hat{\mathbf{F}}_i$. Eq. 5 is essentially the
 576 probability that the training and the target galaxies having
 577 the same SED but at a different redshift. The flux prediction
 578 $p(\mathbf{F}|z, z_i, \hat{\mathbf{F}}_i)$ of the training galaxy at redshift z is modeled
 579 via a Gaussian process,

$$580 \quad F_b \sim \mathcal{GP} \left(\mu^F, k^F \right), \quad (6)$$

581 with mean function μ^F and kernel k^F , both imposed to
 582 capture expected correlations resulting from the known un-
 583 derlying physics (i.e., fluxes resulting from observing SEDs
 584 through filter response, and the SEDs being redshifted). The
 585 reader should refer to Leistedt & Hogg (2017) for further de-
 586 tails.

587 In this study, all 100 ordered Buzzard templates, as
 588 described in Section 2.1.2, were used in DELIGHT, and the
 589 Gaussian process was trained with a subset of 50 000 galax-
 590 ies. Photometric uncertainties from the inputs are propa-
 591 gated into the code, while non-detections for each band are
 592 set to the mean of the respective bands. Default settings
 593 of DELIGHT were used, with the exception that the PDF bins
 594 were set to be linear instead of logarithmic, with 200 equally-
 595 spaced bins between $0.0 < z < 2.0$. In this study a flat prior
 596 is assumed.

597 3.2.4 FlexZBoost

598 FLEXZBOOST¹² (Izbicki & Lee 2017) is a particular realiza-
 599 tion of FlexCode, which is a general-purpose methodology
 600 for converting any conditional mean point estimator of z to
 601 a conditional density estimator $f(z|\mathbf{x})$, where \mathbf{x} here repre-
 602 sents our photometric covariates and errors.¹³ The key idea
 603 is to expand the unknown function $f(z|\mathbf{x})$ in an orthonormal
 604 basis $\{\phi_i(z)\}_i$:

$$605 \quad f(z|\mathbf{x}) = \sum_i \beta_i(\mathbf{x}) \phi_i(z). \quad (7)$$

606 By the orthogonality property, the expansion coefficients are
 607 just conditional means

$$608 \quad \beta_i(\mathbf{x}) = \mathbb{E} [\phi_i(z)|\mathbf{x}] \equiv \int f(z|\mathbf{x}) \phi_i(z) dz. \quad (8)$$

609 These coefficients can easily be estimated from data by re-
 610 gression.

611 In this paper, we use XGBOOST (Chen & Guestrin 2016)
 612 for the regression part as these techniques scale well for mas-
 613 sive data; it should however be noted that FLEXCODE-RF
 614 (also on GitHub), based on Random Forests, generally per-
 615 forms better for smaller data sets. As our basis, we choose a
 616 standard Fourier basis. There are two tuning parameters in
 617 our $p(z)$ estimate: (i) the number of terms, I , in the series
 618 expansion in Eq. 7, and (ii) an exponent α that we use to
 619 sharpen the computed density estimates $\hat{f}(z|\mathbf{x})$, according

¹² <https://github.com/tpospisil/flexcode>;
<https://github.com/rizbicki/FlexCoDE>

¹³ Instead of $p(z)$, we use the notation $f(z|\mathbf{x})$ to explicitly show the dependence on \mathbf{x} .

¹¹ <https://github.com/ixkael/Delight>

8 LSST Dark Energy Science Collaboration

to $\tilde{f}(z|\mathbf{x}) \propto \hat{f}(z|\mathbf{x})^\alpha$. We split the “train data” into a training set (85%) and a validation set (15%), and choose both I and α in an automated way by minimizing the weighted L_2 -loss function (Eq. 5 in Izbicki & Lee 2017) on the validation set.

Although FlexCode offers a *lossless compression* of the photo-z estimates (in this study, one can reconstruct $\tilde{f}(z|\mathbf{x})$ exactly at any resolution from estimates of the first 35 coefficients, Eq. 8, for a Fourier basis $\{\phi_i(z)\}_i$), we discretize our final estimates into 200 bins linearly spaced in $0 < z < 2$ for easy comparison with other algorithms. Using a higher resolution may yield better results (with no added cost in storage).

3.2.5 GPz

GPz¹⁴ (Almosallam et al. 2016a,b) is a sparse Gaussian process based code, a fast and a scalable approximation of full Gaussian Processes (Rasmussen & Williams 2006), with the added feature of being able to produce input-dependent variance estimations (heteroscedastic noise). The model assumes that the probability of the output y , the redshift, given the input x , the photometry, is $p(y|x) = \mathcal{N}(y|\mu(x), \sigma(x)^2)$. The mean function, $\mu(x)$, and the variance function $\sigma(x)^2$ are both linear combinations of basis functions that take the following form:

$$f(x) = \sum_{i=1}^m \phi_i(x) w_i, \quad (9)$$

where $\{\phi_i(x)\}_{i=1}^m$ and $\{w_i\}_{i=1}^m$ are sets of m basis functions and their associated weights respectively. Basis function models (BFM), for specific classes of basis functions such as the sigmoid or the squared exponential, have the advantage of being universal approximators, i.e. there exist a function of that form that can approximate any function, with mild assumptions, to any desired degree of accuracy. The details on how to learn the parameters of the model and the hyper-parameters of the basis functions are described in Almosallam et al. (2016b).

A unique feature in GPz, is that the variance estimate is composed of two terms each quantifying a different source of uncertainty. One term (the model uncertainty) reflects how much of the uncertainty is due to lack of training samples at the location of interest, whereas the second term (the noise uncertainty) reflects how much of the uncertainty is caused from observing many noisy samples at that location. Thus, the predictive variance can determine whether we need more representative samples or more precise samples for any particular location in the input space. GPz can also emphasize the importance of some samples as weights. This weight can be for example $|z_{\text{spec}} - z_{\text{phot}}|/(1 + z_{\text{spec}})$ to target the desired objective of minimizing the normalized redshift error or as a function of their probability in the test set relative to the training set in order to pressure the model to better fit samples that are rare in the training set but are expected to be abundant during testing.

The data is prepared for GPz by taking the log of the magnitude errors, decorrelating the data set using PCA and

imputing the missing values using a simple linear model that estimates the missing variables given the observed ones. The log transformation helps to smooth the long tail distribution of the magnitude errors, which is more stable numerically and makes the optimization process unconstrained. The missing values are imputed by computing the mean of the training set μ and its covariance Σ , then we use the following equation to estimate the missing values from the observed ones

$$x_u = \mu_u + \Sigma_{uo}\Sigma_{oo}^{-1}(x_o - \mu_o), \quad (10)$$

where the subscript o in x_o indexes the *observed* part of the input x , whereas the subscript u indexes the *unobserved* set (similarly for μ and Σ). This is the optimal expected value of the unobserved variables given the observed ones if the distribution is jointly Gaussian, note that if the variables are independent, i.e. $\Sigma_{uo} = 0$, this will reduce to a simple average predictor.

We use the Variable Covariance (VC) option in GPz with 200 basis functions after we note that there is no significant increase in the performance on the validation set (using 80%-20% training-validation split) and with no cost-sensitive learning applied.

3.2.6 METAPHOR

METAPHOR (Machine-learning Estimation Tool for Accurate Photometric Redshifts, Cavuoti et al. 2017a) is a pipeline designed to provide photo-z’s point estimates and a reliable PDF for machine learning (ML) based techniques. It includes pre- and post-processing phases, hosting a photo-z prediction engine based on the Multi Layer Perceptron with Quasi Newton Algorithm (MLPQNA), already validated on photo-z’s in several cases (de Jong et al. 2017; Cavuoti et al. 2017b, 2015; Brescia et al. 2014, 2013; Biviano et al. 2013). Due to its plug-in based modular nature, METAPHOR can be easily replaced by any other photo-z prediction kernel, regardless its implementation, by taking the I/O interface compliance as unique constrain.

At a higher level, the pipeline mainly consists of three modules: (i) *data pre-processing*, including a catalogue cross-matching sub-module (based on the tool C3, Riccio et al. 2017), a sub-module for photometric evaluation and error estimation of the multi-band catalogue used as Knowledge Base (KB), and a sub-module dedicated to the perturbation of the photometric KB, propaedeutic to the PDF estimation; (ii) *photo-z prediction*, which is the training/validation/test phase, producing the photo-z’s point estimates, based on a pre-selected ML method; (iii) *PDF estimation*, specifically designed to calculate the PDF of the photo-z estimation errors. The last module includes also a post-processing tool, providing some statistics on the produced point estimates and PDFs.

The photometry perturbation law is based on the formula $m_{ij} = m_{ij} + \alpha_i F_{ij} * u_{\mu=0, \sigma=1}$, where α_i is a user selected multiplicative constant (useful in case of multi-survey photometry), $u_{\mu=0, \sigma=1}$ is a random value from the standard normal distribution and F_{ij} is a bimodal function (a constant function + polynomial fitting of the mean magnitude errors on the binned bands), heuristically tuned in such a way that the constant component is the threshold under which

¹⁴ <https://github.com/OxfordML/GPz>

733 the polynomial function is considered too low to provide a
 734 significant noise contribution to the photometry perturba-
 735 tion.

736 As introduced, the photo- z point estimate prediction
 737 engine of METAPHOR is based on the MLPQNA model,
 738 whose photo- z regression training error, used by the quasi
 739 Newton learning rule, is based on the least square error and
 740 Tikhonov L_2 -norm regularization (Hofmann & Mathé 2018).

741 As main prerogative, METAPHOR is able to provide
 742 a PDF for ML methods by taking into account the photo-
 743 metric errors provided with data, by running N trainings on
 744 the same training set, or M trainings on M different ran-
 745 dom extractions from the KB. The different test sets, used to
 746 produce the PDF, are thus obtained by introducing a proper
 747 perturbation, parametrized from the photometric error dis-
 748 tribution in each band, on the photometric data populating
 749 the original test set (Brescia et al. 2018).

750 For the present work since it was required to produce
 751 a redshift (and a PDF) for each object of the test set we
 752 decided to apply a hierarchical kNN to fill the missing de-
 753 tection, it goes without saying that for such points the re-
 754 liability of PDFs and point estimation is lower. No cross
 755 validation has been used.

756 3.2.7 SkyNet

757 SKYNET¹⁵ (Graff et al. 2014) is a publicly available neural
 758 network software, based on a 2nd order conjugate gradient
 759 optimization scheme (see Graff et al. 2014, for further de-
 760 tails). It has been used efficiently for redshift PDF estimates
 761 (Sánchez et al. 2014; Bonnett 2015; Bonnett et al. 2016).

762 The neural network is configured as a standard multi-
 763 layer perceptron with three hidden layers and one input layer
 764 with 12 nodes (the 6 magnitudes and their errors). The clas-
 765 sifier is laid out such that the hidden layers have 20:40:40
 766 nodes each, all rectified linear units, and the output layer
 767 has 200 nodes (corresponding to 200 bins for the PDF) acti-
 768 vated with a “softmax” function so that they automatically
 769 sum to 1.

770 To avoid over-fitting, a 30 per cent fraction of the train-
 771 ing set is used as validation, and the training is stopped as
 772 soon as the error rate begins to increase in the validation
 773 set. The weights are randomly initialized based on normal
 774 sampling. The error function is a standard chi-square func-
 775 tion for the regressor, and a cross-entropy function for the
 776 classifier. Finally, the data are all whitened before process-
 777 ing, with magnitudes pegged to (45,45,40,35,42,42) and their
 778 errors pegged to (20,20,10,5,15,15) for *ugrizy* filters, respec-
 779 tively.

780 3.2.8 TPZ

781 TPZ¹⁶ (Trees for Photo- z , Carrasco Kind & Brunner 2013;
 782 Carrasco Kind & Brunner 2014) is a parallel machine learn-
 783 ing algorithm that generates photometric redshift PDFs us-
 784 ing prediction trees and random forest techniques. The code
 785 recursively splits the input data (i. e. the training sample),
 786 into two branches, one after another, until a terminal leaf is

787 created that meets a termination criterion (e. g. a minimum
 788 leaf size or a variance threshold). Bootstrap samples from
 789 the training data and associated errors are used to build a
 790 set of prediction trees. In order to minimize correlation be-
 791 between the trees, the data is divided in such a way that the
 792 highest information gain among the random subsample of
 793 features is obtained at every point. The regions in each ter-
 794 minal leaf node corresponds to a specific subsample of the
 795 entire data that possesses similar properties.

796 The training data is examined before running TPZ.
 797 Since TPZ does not handle non-detections (magnitudes
 798 flagged as 99.0), we replace these values with an approxi-
 799 mation of the 1σ detection threshold, i. e. a signal to noise
 800 ratio of 1 in terms of magnitude uncertainty using the equa-
 801 tion $dm = 2.5 \log(1 + N/S)$ where $dm \sim 0.7526 \text{ mag}$
 802 for $N/S = 1$. That is, for each band, we replace the non-
 803 detection with the magnitude corresponding to the error of
 804 0.7526 from the error model forecasted for 10-year LSST
 805 data. The Out-of-Bag (Breiman et al. 1984; Carrasco Kind
 806 & Brunner 2013) cross-validation technique is used within
 807 TPZ to evaluate its predictive validity and determine the
 808 relative importance of the different input attributes. We em-
 809 ployed this information to calibrate our algorithm.

810 In the present work, the LSST magnitudes u , g , r , i
 811 and colors $u-g$, $g-r$, $r-i$, $i-z$, $z-y$ and their associated
 812 errors are used in the process of growing 100 trees with a
 813 minimum leaf size of 5 (the z and y magnitudes did not
 814 show significant correlation with the redshift in our cross-
 815 validation, so we did not use them when constructing our
 816 trees). We partitioned our redshift space into 100 bins from
 817 $z = 0.005$ to $z = 2.0$ and smoothed each individual PDF
 818 with a smoothing scale of twice the bin size.

819 3.3 Simple Ensemble Estimator

820 In addition to the main photo- z algorithms described above
 821 we also include a very simple method. For TRAINZ, as we will
 822 we call this simple estimator, we well define $p(z)$ as simply:

$$823 p(z) = \frac{1}{N_{train}} \sum_{i=1}^{N_{train}} z_{train} \quad (11)$$

824 That is, we simply set the redshift PDF of every galaxy equal
 825 to the normalized $N(z)$ of the training sample. As the train-
 826 ing sample is drawn from the same underlying distribution
 827 as the test sample, modulo small deviations due to sam-
 828 ple size, the quantiles of the training and test distributions
 829 should be identical. This is a wildly unrealistic estimator, as
 830 it assigns all galaxies, no matter their apparent magnitude,
 831 colour, or true redshift, the same redshift PDF, and is thus
 832 uninformative at the level of individual object redshifts, but
 833 is designed to perform very well for the ensemble of all ob-
 834 jects. We will discuss this method and cautions relative to
 835 metrics in Section 5.3.

836 4 METRICS FOR QUANTIFYING PDF 837 COMPARISONS

838 The overloaded “ $p(z)$ ” is a widespread abuse of notation;
 839 we would like the outputs of photo- z PDF codes to be in-
 840 terpretable as probabilities. Obviously photo- z PDFs must

15 <http://ccpforge.cse.rl.ac.uk/gf/project/skynet/>

16 <https://github.com/mgckind/MLZ>

not take negative values and must integrate to unity over the range of possible redshifts. Additionally, an estimator derived by method H for the photo- z PDF of galaxy i must be understood as a posterior probability distribution

$$\hat{p}_j(z_i) = p(z|d_i, I_D, I_H), \quad (12)$$

conditioned not only on the photometric data d_i for that galaxy but also on parameters encompassing a number of things that will differ depending on the method H used to produce it, namely the assumptions I_H necessary for the method to be valid and any inputs I_D it takes as prior information, such as a template library or training set. Because of this, direct comparison of photo- z PDFs produced by different methods is in some sense impossible; even if they share the same prior information I_D , by definition they cannot be conditioned on the same assumptions I_H , otherwise they would not be distinct methods at all.

In this study, we isolate the differences in prior information specific to each method by using a single training set I_D^{ML} for all machine learning-based codes and a single template library I_D^T for all template-based codes, and these sets of prior information are carefully constructed to be representative and complete, we have $I_D^{ML} \equiv I_D^T$ for every method H . Thus, we are saying

$$\frac{\hat{p}_{i,H}(z)}{\hat{p}_{i,H'}(z)} \approx \frac{p(z|d_i, I_H)}{p(z|d_i, I_{H'})}, \quad (13)$$

meaning that we assume comparisons of $\hat{p}_{i,H}(z)$ isolate the effect of the method used to obtain the estimator, which should make examination of differences caused by specifics of the method implementations easier to isolate.

As mentioned previously, there are cosmology probes that require knowledge of individual galaxy $p(z)$ and others that require only knowledge of the ensemble redshift distribution, $N(z)$. Due to the paucity of principled techniques for using and validating photo- z PDFs, there are few alternatives to the common practice of reducing photo- z PDFs to point estimates. Though this practice should not be encouraged, we also calculate traditional metrics based on the most common point estimators derived from photo- z PDFs. Those seeking to establish a connection to traditional ways of thinking about redshift estimation may consult the Appendix for these results.

There are a number of metrics that can be used to test the accuracy of a photo- z interim posterior as an estimator of a true photo- z posterior if it is known. Even for simulated data, the true photo- z PDF is in general not accessible unless the redshifts are in fact drawn from the true photo- z PDFs, a mock catalogue generation procedure that has not yet appeared in the literature. Furthermore, only limited applications of photo- z PDFs that could be used as the basis for a metric have been presented in the literature. The most popular application by far is the calculation of the overall redshift distribution $N(z)$, the true value of which is known for the BUZZARD simulation and will be denoted as $N'(z)$. Though alternatives exist (Malz & Hogg prep), stacking according to

$$\hat{N}^H(z) \approx \frac{1}{N_{tot}} \sum_i^{N_{tot}} \hat{p}_i^H(z) \quad (14)$$

is the most widely accepted method for estimating the redshift distribution from photo- z PDFs. If we assume that the response of estimators of $N(z)$ is uniform across all approaches H , then we may interpret metrics on the accuracy of $\hat{N}(z)$ obtained in this way. We must note, however, that this is a poor assumption in general. Under the setup of this paper, the true redshift distribution $N'(z) = p(z|I_D)$ (i.e. because our training data is representative, the interim prior is the truth). In this ideal case, the method that would give the best approximation to $N'(z)$ would be one that neglects all the information contained in the photometry $\{d_i\}_{N_{tot}}$ and gives every galaxy the same photo- z PDF $\hat{p}_i(z) = N'(z)$ for all i . This is the exact estimator, TRAINZ, that we have described in Section 3.3, and which will serve as a point of reference for the other codes.

The exact implementation of the stacked estimator $\hat{N}^H(z)$ will depend on the parametrization of the photo- z PDFs, which may differ across codes and can affect the precision of the estimator (Malz et al. 2018); even considering a single method under the same parametrization, say a piecewise constant function over bins or a set of samples from the posterior, an estimator using $2N$ bins or samples will trivially be more precise than an estimator using N bins or samples. In order to minimize the effects of such choices, we asked those running all eleven codes to output $p(z)$ parameterized with a generous ≈ 200 piecewise constant bins spanning $0 < z < 2$. The piecewise constant format is chosen because of its established presence in the literature, and the choice of 200 bins was motivated by the approximate number of columns expected to be available for storage of $p(z)$ for the final LSST Project tables.¹⁷ All $p(z)$ catalogues are processed using the QP software package (Malz et al. 2018)¹⁸ for manipulating and calculating metrics of 1-dimensional PDFs. We will discuss the choice of $p(z)$ parameterization further in Section 5.

4.1 Metrics of an ensemble of photo- z interim posteriors

4.1.1 Probability integral transform (PIT)

The probability integral transform (PIT) (Polsterer et al. 2016) is defined for each individual galaxy as:

$$\text{PIT} = \int_{-\infty}^{z_{\text{true}}} p(z) dz. \quad (15)$$

The distribution of PIT values quantifies the behavior of the ensemble of photo- z PDFs, enabling us to evaluate whether the $p(z)$ is, on average, accurate: The PIT value is the Cumulative Distribution Function (CDF) of the $p(z)$ evaluated at the true redshift. A catalogue of photo- z PDFs that are accurate should have a flat PIT histogram (i.e., the individual PIT values as samples from each CDF should match a Uniform(0,1) distribution if the CDFs are accurate). Specific deviations from flatness indicate inaccuracy: overly broad photo- z PDFs would manifest as underrepresentation of the

¹⁷ See, e. g. the LSST Data Products Definition Document, available at: <https://ls.st/dpdd>

¹⁸ available at: <http://github.com/aimalz/qp/>

lowest and highest PIT values, whereas overly narrow photo-
¹⁰⁰¹
⁹⁴⁸
^z PDFs would manifest as over-representation of the lowest
¹⁰⁰²
⁹⁴⁹ and highest PIT values. High frequency at only $\text{PIT} \approx 0$
¹⁰⁰³
⁹⁵⁰ and $\text{PIT} \approx 1$ indicates the presence of catastrophic outliers
¹⁰⁰⁴
⁹⁵¹ with highly inaccurate photo- z PDFs where the true red-
¹⁰⁰⁵
⁹⁵² shift is outside of the support of $p(z)$. Tanaka et al. (2017)
¹⁰⁰⁶
⁹⁵³ use the histogram of PIT values as a diagnostic indicator of
¹⁰⁰⁷
⁹⁵⁴ overall code performance, while Freeman et al. (2017) inde-
¹⁰⁰⁸
⁹⁵⁵ pendently define the PIT and demonstrate how its individ-
¹⁰⁰⁹
⁹⁵⁶ ual values may be used both to perform hypothesis testing
¹⁰¹⁰
⁹⁵⁷ (via, e.g., the KS, CvM, and AD tests; see below) and to
¹⁰¹¹
⁹⁵⁸ construct quantile-quantile plots.
¹⁰¹²
⁹⁵⁹

4.1.2 Quantile-quantile (QQ) plot

The quantile-quantile (QQ) plot is a graphical method for
¹⁰¹⁴
⁹⁶⁰ comparing two distributions, where the quantiles of one dis-
¹⁰¹⁵
⁹⁶¹ tribution are plotted against the quantiles of the other distri-
¹⁰¹⁶
⁹⁶² bution (A quantile being defined by partitioning a distribu-
¹⁰¹⁷
⁹⁶³ tion into consecutive intervals containing equal amounts of
¹⁰¹⁸
⁹⁶⁴ probability, or equal numbers of objects in each interval). In
¹⁰¹⁹
⁹⁶⁵ this paper we show the quantiles of the PIT values compared
¹⁰²⁰
⁹⁶⁶ to the quantiles of the Uniform distribution that we expect
¹⁰²¹
⁹⁶⁷ the PIT values to match if $p(z)$ is an accurate probability dis-
¹⁰²²
⁹⁶⁸ tribution for all objects. The QQ plot provides an easy way
¹⁰²³
⁹⁶⁹ to qualitatively assess the differences in various properties
¹⁰²⁴
⁹⁷⁰ such as the moments of an estimating distribution relative
¹⁰²⁵
⁹⁷¹ to a true distribution. In this paper, QQ plots are used for
¹⁰²⁶
⁹⁷² two purposes: (1) for comparing $N(z)$ from photo- z PDFs
¹⁰²⁷
⁹⁷³ (estimated using Eq. 14) with the true $N(z)$, i.e. comparing
¹⁰²⁸
⁹⁷⁴ the estimated distribution of redshifts with the true redshift
¹⁰²⁹
⁹⁷⁵ distribution, and (2) for assessing the overall consistency of
¹⁰³⁰
⁹⁷⁶ an ensemble of photo- z PDFs with their true redshifts on
¹⁰³¹
⁹⁷⁷ a population level, where the distribution of the PIT values
¹⁰³²
⁹⁷⁸ (see previous section) is compared to a uniform distribution
¹⁰³³
⁹⁷⁹ between 0 and 1. The QQ plot contains very similar infor-
¹⁰³⁴
⁹⁸⁰ mation to that shown in the PIT histogram plot, we include
¹⁰³⁵
⁹⁸¹ both forms, as visually they each convey the information in
¹⁰³⁶
⁹⁸² a somewhat distinct manner.
¹⁰³⁷
⁹⁸³

4.1.3 Conditional density estimation loss

With the conditional density estimation loss (CDE loss) we
¹⁰³⁸
⁹⁸⁶ can compare how well different methods estimate individual
¹⁰³⁹
⁹⁸⁷ PDFs for photometric covariates \mathbf{x} rather than looking only
¹⁰⁴⁰
⁹⁸⁸ at the ensemble distribution. As in Section 3.2.4, we use
¹⁰⁴¹
⁹⁸⁹ the notation $f(z|\mathbf{x})$ instead of $p(z)$ to explicitly show the
¹⁰⁴²
⁹⁹⁰ dependence on \mathbf{x} .
¹⁰⁴³
⁹⁹¹

The CDE loss is defined as:

$$L(f, \hat{f}) = \int \int (f(z|\mathbf{x}) - \hat{f}(z|\mathbf{x}))^2 dz dP(\mathbf{x}) \quad (16)$$

This loss is the CDE equivalent of the RMSE in regression.
¹⁰⁴⁴
⁹⁹⁴ To estimate this loss we rewrite the loss as

$$\mathbb{E}_{\mathbf{X}} \left[\int \hat{f}(z|\mathbf{X})^2 dz \right] - 2\mathbb{E}_{\mathbf{X}, Z} \left[\hat{f}(Z|\mathbf{X}) \right] + K_f, \quad (17)$$

where the first expectation is with respect to the marginal
¹⁰⁴⁵
⁹⁹⁵ distribution of the covariates \mathbf{X} , the second expectation is
¹⁰⁴⁶
⁹⁹⁶ with respect to the joint distribution of \mathbf{X} and Z , and K_f is a
¹⁰⁴⁷
⁹⁹⁷ constant depending only upon the true conditional densities
¹⁰⁴⁸
⁹⁹⁸

$f(z|\mathbf{x})$. For each method we can estimate these expecta-
¹⁰⁴⁹
⁹⁹⁹ tions as empirical expectations on the test or validation data
¹⁰⁵⁰
¹⁰⁰⁰ (Eq. 7 in Izbicki et al. 2017) without knowledge of the true
¹⁰⁰¹
¹⁰⁰² densities.

4.2 Metrics over estimated probability distributions

In tandem with the QQ and PIT metrics introduced above, we additionally compute the following metrics comparing the empirical CDF of a distribution to the true or expected distribution. These metrics give a more quantitative measure of the departure from ideal than the more visual PIT histogram and QQ plot. We compute metrics comparing the CDF of PIT values to a the CDF of a Uniform distribution, and also compute the CDF of the true redshift distribution $N'(z)$ compared the $\hat{N}(z)$ distribution derived from summing the $p(z)$ as described in Eq. 14.

4.2.1 Root-mean-square error (RMSE)

We employ the familiar root-mean-square error:

$$\text{RMSE} = \sqrt{\int_{-\infty}^{\infty} (\hat{f}(z) - f'(z))^2 dz}, \quad (18)$$

Though this metric does not account for the fact that the redshift distribution function is, in fact, a probability distribution, it can still be interpreted as a measure of the integrated difference between the estimated distribution and the true distribution, and it can be used to quantify the otherwise qualitative metrics.

4.2.2 Kolmogorov-Smirnov (KS) and related statistics

The Kolmogorov-Smirnov statistic N_{KS} is the maximum dif-
¹⁰²⁶
⁹⁸² ference between $F_{\text{phot}}(z)$ and $F_{\text{spec}}(z)$, the CDFs of the
¹⁰²⁷
⁹⁸³ photo- z and spectroscopic redshift respectively:

$$N_{\text{KS}} = \max_z (|F_{\text{phot}}(z) - F_{\text{spec}}(z)|). \quad (19)$$

The KS test quantifies the similarity between two distri-
¹⁰³¹
⁹⁸⁴ butions, independent of binning. A lower N_{KS} value corre-
¹⁰³²
⁹⁸⁵ sponds to more similar distributions.

We also consider two variants of the KS statistic: the Cramer-von Mises (CvM) and Anderson-Darling (AD) statistics. The CvM statistic is similar to the KS statistic as it is also computed from the distance between the measured CDF and the ideal CDF, but instead of the maximum distance, the CvM statistic calculates the average of the distance squared:

$$\omega^2 = \int_{-\infty}^{+\infty} (F_{\text{meas.}}(x) - F_{\text{ideal}}(x))^2 dF_{\text{ideal}} \quad (20)$$

The AD statistic is a weighted version of the CvM statistic, making it more sensitive to the tails of the distribution:

$$A^2 = n \int_{-\infty}^{+\infty} \frac{(F_{\text{meas.}}(x) - F_{\text{ideal}}(x))^2}{F_{\text{ideal}}(x)(1 - F_{\text{ideal}}(x))} dF_{\text{ideal}} \quad (21)$$

where n is the sample size.

1046 4.2.3 *Moments*

1047 For the $\hat{N}(z)$ distributions we additionally calculate the first
 1048 three moments of the estimated redshift distribution for each
 1049 code and compare them to the moments of the true redshift
 1050 distribution $N'(z)$. The m th moment of a distribution is
 1051 defined as

$$1052 \quad \langle z^m \rangle = \int_{-\infty}^{\infty} z^m N(z) dz. \quad (22)$$

1053 Here, we use the moments of the stacked estimator of the
 1054 redshift distribution function as the basis for a metric. The
 1055 closer the moments of $\hat{N}(z)$ for a photo-z PDF method are
 1056 to the moments of the true redshift distribution function
 1057 $N'(z)$, the better the photo-z PDF method.

1058 5 RESULTS

1059 5.1 Ensembles of photo-z interim posteriors

1060 Fig. 1 Shows the $p(z)$ produced by each of our eleven photo-
 1061 z codes for four example galaxies which exemplify some
 1062 prominent cases that arise when estimating photo-z PDFs: a
 1063 narrow, unimodal redshift solution, a broader unimodal so-
 1064 lution, a bimodal distribution, and a complex, multimodal
 1065 distribution. The red vertical line represents the true red-
 1066 shift of the individual galaxy, and the blue curve repre-
 1067 sents the redshift probability. Several features are obvious
 1068 even in these illustrative examples. ANNz2, METAPHOR,
 1069 NN, and SKYNET all show an excess of small-scale features,
 1070 which appear to be print-through of the underlying train-
 1071 ing set galaxies. GPZ (in its current implementation), on
 1072 the other hand, always produces a single Gaussian, which
 1073 broadens to cover the multi-modal redshift solutions seen in
 1074 other codes.

1075 As stated in Section 4, $p(z)$ is parameterized as ≈ 200
 1076 piecewise constant bins covering $0 < z < 2$ for all eleven
 1077 codes, giving a grid size of roughly $\delta z = 0.01$ for each code.
 1078 A piecewise constant grid was a natural choice for some
 1079 photo-z codes, for instance most template-based codes com-
 1080 pute likelihoods on a fixed grid. In contrast, FlexZBoost, for
 1081 example, can return estimates on any grid without compres-
 1082 sion errors as its a basis expansion method where only the
 1083 expansion coefficients need to be stored. Codes with a na-
 1084 tive output format other than the shared piecewise constant
 1085 binning scheme (or one that can be losslessly converted to
 1086 it) may suffer from loss of information when converting to
 1087 it, which could artificially favor some codes over others.

1088 Furthermore, the fidelity of photo-z interim posteriors
 1089 in this format varies with the quality of the photometry. For
 1090 faint galaxies, this redshift resolution is sufficient to capture
 1091 the shape of $p(z)$ for the majority of the test sample, where
 1092 photometric errors on the faint galaxies lead to somewhat
 1093 broad peaks in the redshift posterior. However, as can be
 1094 seen in e. g. the top left panel of Fig. 1, for bright galaxies
 1095 with narrow $p(z)$ the grid spacing of $\delta z = 0.01$ is not suffi-
 1096 cient to resolve the peak. This is consistent with the results
 1097 described in Malz et al. (2018), who find that quantiles (and,
 1098 to a lesser degree, samples) often outperform gridded $p(z)$,
 1099 particularly for bright objects and in the presence of harsher
 1100 storage constraints. With a full 200 numbers to capture the

1101 information of each photo-z PDF, any parametrization will
 1102 perform adequately, but other storage parametrizations and
 1103 limits on storage resources may be considered in future work.
 1104 We will discuss this further in Section 6.

1105 Fig. 2 shows both the quantile-quantile plots (red)
 1106 and the histogram of PIT values (blue) summarizing the results
 1107 from each photo-z code. The red line shows the measured
 1108 quantiles, while the black diagonal represents the ideal QQ
 1109 values if the distribution were perfectly reproduced. A sec-
 1110 ond panel below the main panel for each code shows the dif-
 1111 ference between Q_{data} and Q_{theory} , i. e. the departure from
 1112 the diagonal, for clarity. Biases and trends in whether the
 1113 average width of the $p(z)$ values being over/under-predicted
 1114 are evident. An overall bias where the predicted redshift
 1115 is systematically low manifests as the measured QQ value
 1116 falling above the diagonal, as is the case for BPZ and EAZY,
 1117 while a systematic overprediction shows up as the measured
 1118 QQ value falling below the diagonal, as seen in TPZ. In
 1119 terms of PIT histograms, a systematic underprediction of
 1120 redshift corresponds to fewer PIT values at $PIT < 0.5$ and
 1121 more at $PIT > 0.5$, while a systematic overprediction will
 1122 show the opposite.

1123 Examination of the PIT histograms and QQ plots shows
 1124 that there are fairly generic issues with the width of $p(z)$ un-
 1125 certainty: DELIGHT, NN, SKYNET and TPZ all show a PIT
 1126 histogram with an dearth of low values and an excess of high
 1127 values, signs that, on average, their $p(z)$ are more
 1128 broad than the true distribution of redshifts. METAPHOR
 1129 shows the opposite trend, indicating the $p(z)$ are more
 1130 narrow than the distributions given by the true redshifts.
 1131 In all of these code cases there is a free parameter or band-
 1132 width that can be used to tune uncertainties. The sensitivity
 1133 of multiple codes to this bandwidth choice emphasizes the
 1134 fact that great care must be taken in setting user-defined
 1135 parameters in photo-z codes, even in the presence of rep-
 1136 resentative training/validation data. for FLEXZBOOST the
 1137 “sharpening” parameter (described in Section 3.2.4) plays
 1138 a key role in improving the results, resulting in a QQ plot
 1139 that is very nearly diagonal. A similar sharpening procedure
 1140 could be beneficial for several codes. Interestingly, the three
 1141 purely template-based codes, BPZ, EAZY, and LEPHARE,
 1142 show relatively well behaved $p(z)$ statistics (albeit with some
 1143 bias), which may indicate that the likelihood estimation with
 1144 representative templates is accurately capturing the uncer-
 1145 tainties on individual redshifts.

1146 The ideal PIT histogram would follow the black dashed
 1147 line, representing a uniform distribution of PIT values,
 1148 equivalent to the diagonal line in the QQ plot. Overly broad
 1149 $p(z)$ values show up as an excess of PIT values near 0.5
 1150 and a dearth of values at the edges, while overly narrow
 1151 $p(z)$ will have an excess at the edges and will be missing
 1152 values at the centre. Another feature evident in the PIT
 1153 histograms is the number of “catastrophic outlier” values
 1154 where the true redshift falls outside of the non-zero support
 1155 of $p(z)$, corresponding to $PIT = 0.0$ or 1.0 is more apparent
 1156 than in the QQ plots. Following Kodra & Newman (in prep.)
 1157 we define f_0 as the fraction of objects with $PIT < 0.0001$
 1158 or $PIT > 0.9999$. Table 2 lists these fractions for each of
 1159 the codes. For a proper Uniform distribution we expect a
 1160 value of 0.0002. Several codes show a marked excess, with
 1161 ANNz2, FLEXZBOOST, LEPHARE, AND METAPHOR with
 1162 $f_0 > 0.02$, indicating a sizeable number of catastrophic red-

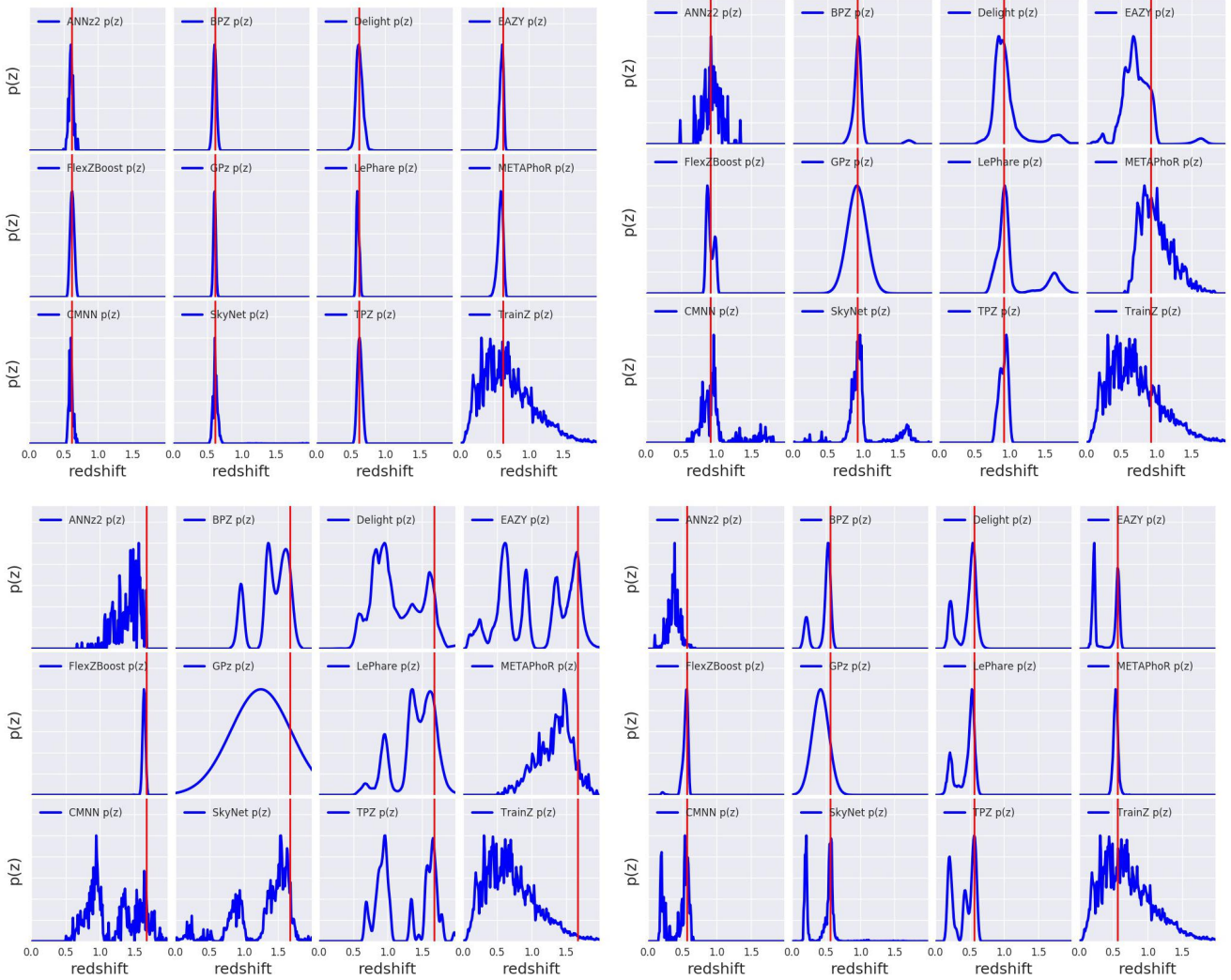


Figure 1. Four illustrative examples of individual $p(z)$ distributions produced by the codes. The red vertical line represents the true redshift. Examples are chosen with common features seen in PDFs: tight unimodal $p(z)$ (upper left), broad unimodal $p(z)$ (upper right), bimodal $p(z)$ (lower right), and complex/multimodal $p(z)$ (lower left). Codes show varying amounts of small-scale structure in their reconstruction of the posterior distribution. We see varying responses from the codes in the presence of color degeneracies and photometric errors, resulting in narrow and broad unimodal, bimodal, and multi-modal $p(z)$ curves.

shift solutions where the true redshift is not covered by the extent of $p(z)$. For METAPHOR this may be partially due to an overall underprediction of the $p(z)$ width, however this is not the case for the other codes. LEPHARE is a particular outlier with nearly 5 per cent of objects outside of $p(z)$ support. Further study will be necessary to determine what is causing these misclassifications for LEPHARE. As expected, and by design, TRAINZ has the proper fraction of outliers for the f_0 statistic.

Fig. 3 shows comparative metric values for the quantitative Kolmogorov-Smirnov (KS), Cramer-Von Mises (CvM), and Anderson Darling (AD) test statistics for each of the codes based on comparing the distribution of their PIT values to the expected uniform distribution over the interval $[0,1]$. The individual values of the statistic are not as important as the comparative score between the different codes. The AD test statistic diverges for values that include the extrema, and thus is calculated by excluding the edges of the

distribution. We calculate the AD statistic over the range of PIT values $v = [0.01, 0.99]$. ANNz2 and FLEXZBOOST score very well for the PIT metrics. METAPHOR and LEPHARE score very well in the PIT AD statistic, but both have a large number of catastrophic outliers, resulting in higher KS and CvM scores.

Given the near-perfect training data, examining the individual codes for explanations for departures from the expected behaviour will be instructive in avoiding similar problems in future tests. ANNz2 performs quite well in $p(z)$ based metrics. In the specific implementation employed in this paper, the final $p(z)$ is a weighted average of five neural-nets. During the training process ANNz2 compares the percentiles of the redshift training sample against the CDFs of the $p(z)$ sample. Distributions that more closely match are given extra weight, and the final weights are designed to produce accurate percentiles. Given that our metrics are focused on the percentile distributions, it is unsurprising that

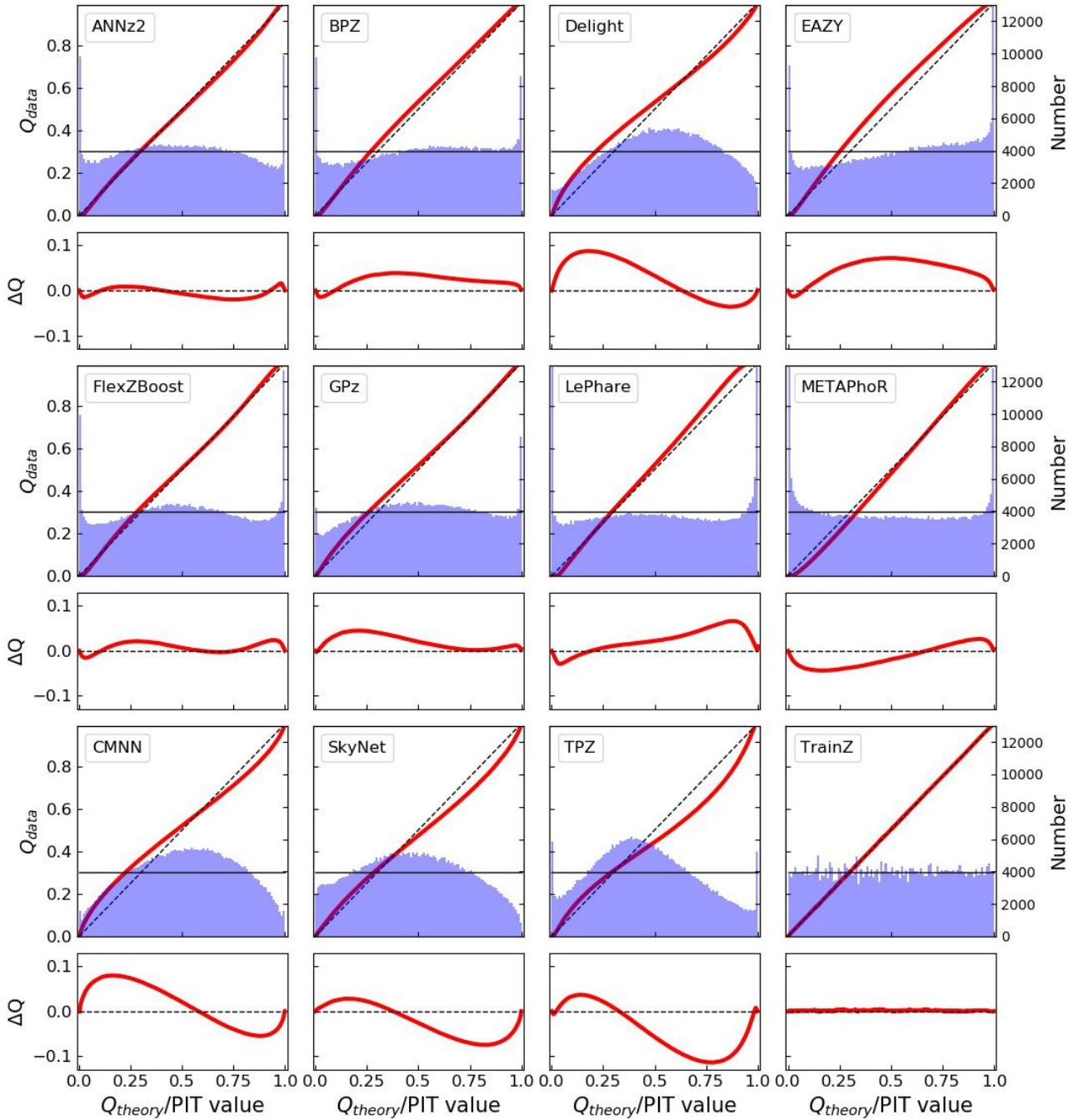


Figure 2. Summary plots for all eleven photo-z codes illustrating performance for the interim posterior statistics. The top panel of each pair shows both the Quantile-Quantile (QQ) plot (red) and the histogram of PIT values (blue). The desired behavior is a QQ plot that matches the diagonal dashed line, and a PIT histogram that matches a uniform distribution matching the thin horizontal black line. The bottom panel of each pair shows the difference between the QQ quantile and the diagonal, illustrating departure from the desired performance. Histograms with an overabundance of PIT values at the centre of the distribution indicate $p(z)$ distributions that are overly broad, while an excess of values at the extrema indicate $p(z)$ distributions that are overly narrow. Values of PIT=0 and PIT=1 indicate “catastrophic failures” where the true redshift is completely outside the support of $p(z)$. Asymmetric features are indicative of systematic bias in the redshift predictions. A variety of behaviors are evident, and specific details are discussed in the text.

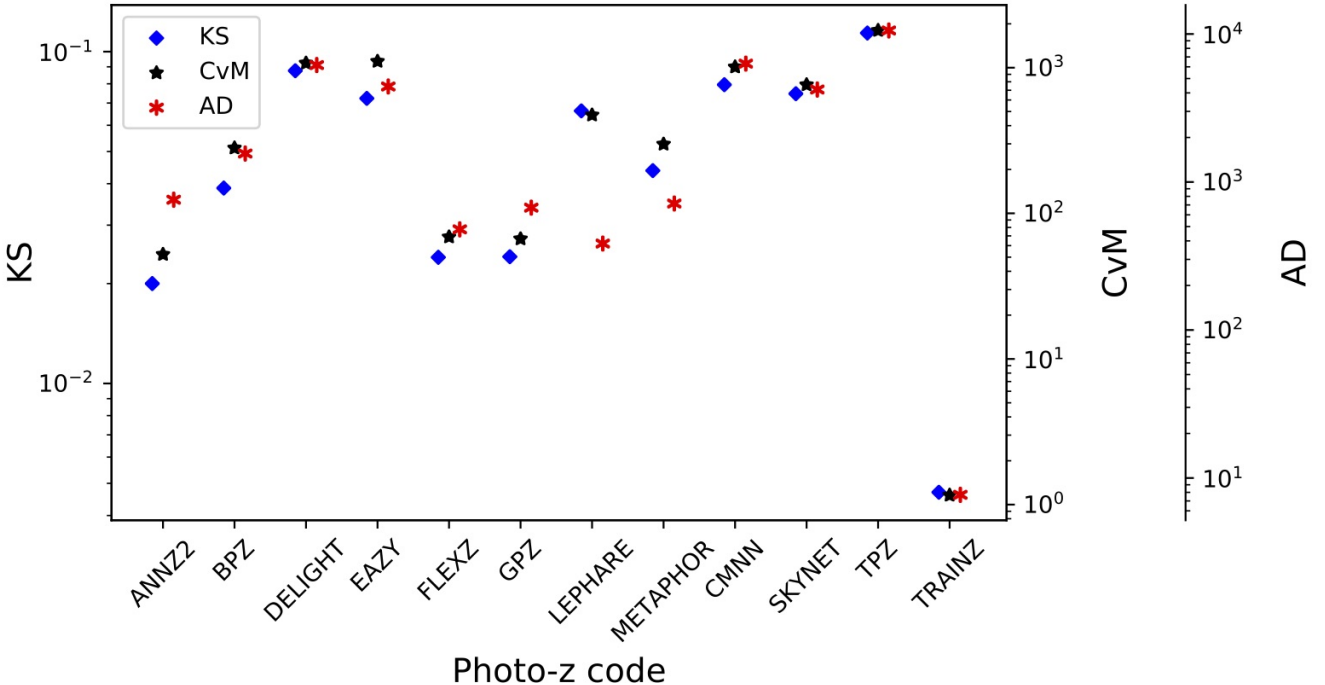


Figure 3. A visual representation of the Kolmogorov-Smirnov (KS, blue diamond), Cramer-von Mises (CvM, black star), and Anderson-Darling (AD, red asterisk) statistics for the PIT distributions. The statistics are often highly correlated, though the AD statistic truncates the extrema of the distribution and can have disparate values compared to KS and CvM.

Table 2. The fraction of “catastrophic outlier” PIT values. We expect a value of 0.0002 for a proper Uniform distribution. An excess over this small value indicates true redshifts that fall outside the non-zero support of the $p(z)$.

Photo-z Code	fraction $\text{PIT} < 10^{-4}$ or > 0.9999
ANNz2	0.0265
BPZ	0.0192
DELIGHT	0.0006
EAZY	0.0154
FLEXZBOOST	0.0202
GPZ	0.0058
LEPHARE	0.0486
METAPHOR	0.0229
CMNN	0.0034
SKYNET	0.0001
TPZ	0.0130
TRAINZ	0.0002

ANNz2 performs well in the given metrics. The discreteness in the individual $p(z)$ estimated by ANNz2 can be attributed to the fact that the code was run as a classifier, assigning weights to discrete bins of redshift. While multiple bins may receive weight, the bins themselves will still be discretized, and no additional smoothing was performed. Overall, FLEXZBOOST and ANNz2 show the best ensemble agreement in their distribution of PIT values.

5.2 Metrics of the stacked estimator of the redshift distribution

Fig. 4 shows the stacked $\hat{N}(z)$ distribution compared to the true redshift distribution $N'(z)$ for all tested codes. The red line indicates the summed $p(z)$ for each code, while the blue line shows the true redshift distribution smoothed via kernel density estimation (KDE), with a bandwidth chosen via Scott’s rule (Scott 1992). While Scott’s rule is used to display $N'(z)$ in the figure, all quantitative statistics are computed via the empirical CDF, and are thus unaffected by bandwidth/smoothing choice. Several of the codes show an excess at $z \sim 1.4$, particularly the template-based codes BPZ, EAZY, and LEPHARE. This is likely due to the 4000 angstrom break passing through the gap between the z and y filters. This feature is one of the most prominent in individual galaxy $p(z)$, and is readily seen in the point-estimate plots shown in Fig. A1 and described in the Appendix. Several of the machine learning based codes appear to be overtrained, adding excess galaxy probability to the redshift peaks and missing probability in the troughs. Given that our training data is drawn from the same galaxy population as the test set, and our data has prominent peaks in $N'(z)$, perhaps it is not unexpected that such overtraining occurs. A more extensive training/validation set might allow for a better choice of smoothing parameters in individual codes that would avoid such overtraining.

As with the $p(z)$ values in Figure 2, different levels of substructure are obvious for the different codes. While Scott’s rule provides a relatively good general smoothing scale to represent the true $N'(z)$, there are smaller scale

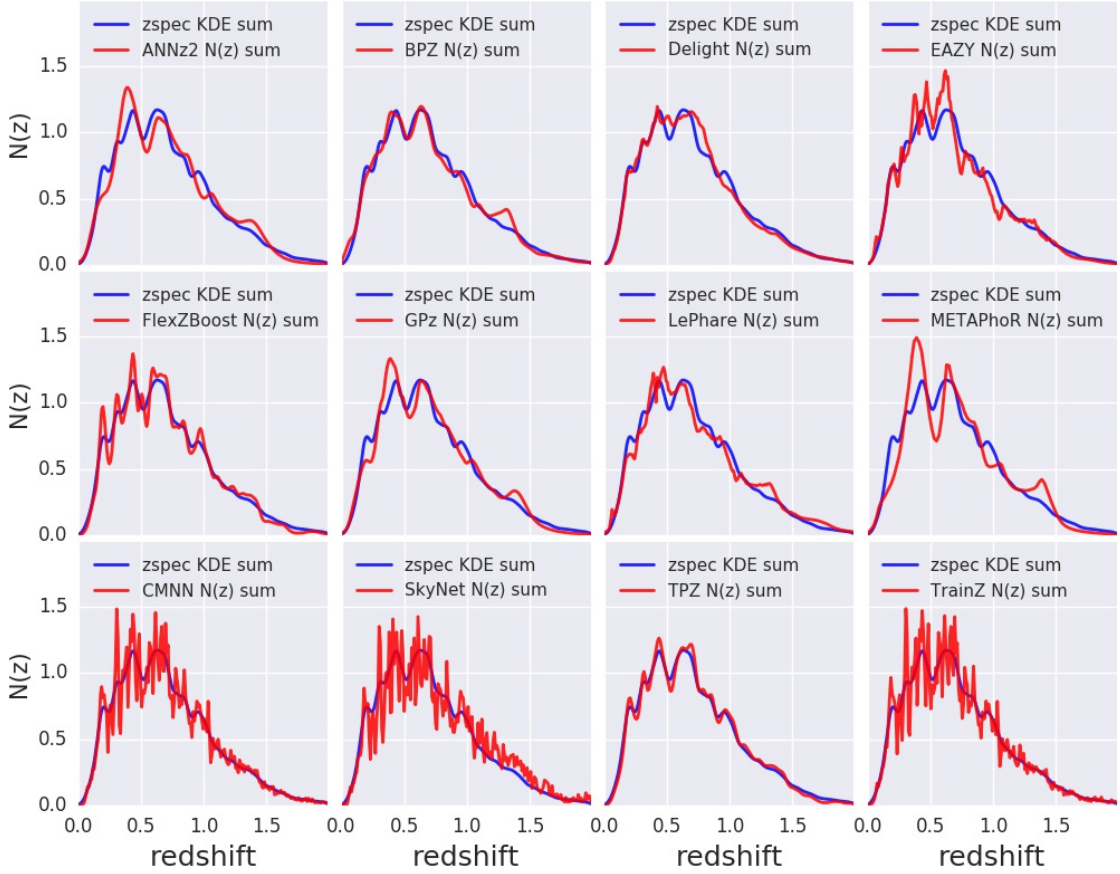


Figure 4. The stacked $p(z)$ produced by each photo- z code ($\hat{N}(z)$, red) compared to the spectroscopic redshift distribution ($N'(z)$, blue). Varying levels of small-scale structure are seen in the codes. $N'(z)$ is smoothed using a single bandwidth chosen via Scott’s rule for all codes.

fluctuations: while FLEXZBOOST and CMNN appear somewhat discrepant in Fig. 4, they are actually the two most accurate in terms of their quantitative measurements. Interestingly, while ANNz2 shows an abundance of small scale structure in individual $p(z)$ measurements (see Fig. 1), the summed $\hat{N}(z)$ is rather smooth, where the small scale features average out. This is not the case for the two other codes that show an abundance of substructure in their individual $p(z)$: both CMNN and SKYNET show small scale features both in $p(z)$ and $\hat{N}(z)$. For CMNN the $p(z)$ are simply a weighted histogram of all spectroscopic training galaxies in nearby colour space with no smoothing applied, so the substructure is not unexpected. The PIT histogram and shape of the QQ plot in Figure 2 show that CMNN is producing $p(z)$ that are overly broad, additional smoothing of the $p(z)$ would exacerbate this problem. While the $\hat{N}(z)$ plot shows more small scale features than other codes, these features are actually representative of real structure in the true $N'(z)$, as evidenced by the very good metric scores for CMNN. SKYNET $p(z)$ were also not smoothed: while previous implementations of the code such as Sánchez et al.

(2014) and Bonnett (2015) (see Appendix C.3) implement a “sliding bin” smoothing, no such procedure was used in this study. In addition to excess substructure, SKYNET shows an obvious redshift bias, evident both visually in Figure 4 and in the first moment of $N(z)$ listed in Table 5, where it is clearly an outlier. SKYNET employed a method where a random sample of training galaxies was chosen, but there was no test that the subset was completely representative of the overall redshift distribution. Also unlike Bonnett (2015), no effort was made to add extra weight to more rare low and high redshift galaxies. Either of these decisions could be the cause of the bias seen in our results. Future runs of SKYNET will explore these implementation choices and their effects.

Figure 5 shows the quantitative Kolmogorov-Smirnoff (KS), Cramer-Von Mises (CvM), and Anderson Darling (AD) test statistics for each of the codes for the $\hat{N}(z)$ based measures. FLEXZBOOST, CMNN, and TPZ outperform the other codes in the $\hat{N}(z)$ metrics. It is unsurprising that CMNN scores well, as with a near perfectly representative training set means that choosing neighbouring points in color/magnitude space should lead to excellent agreement

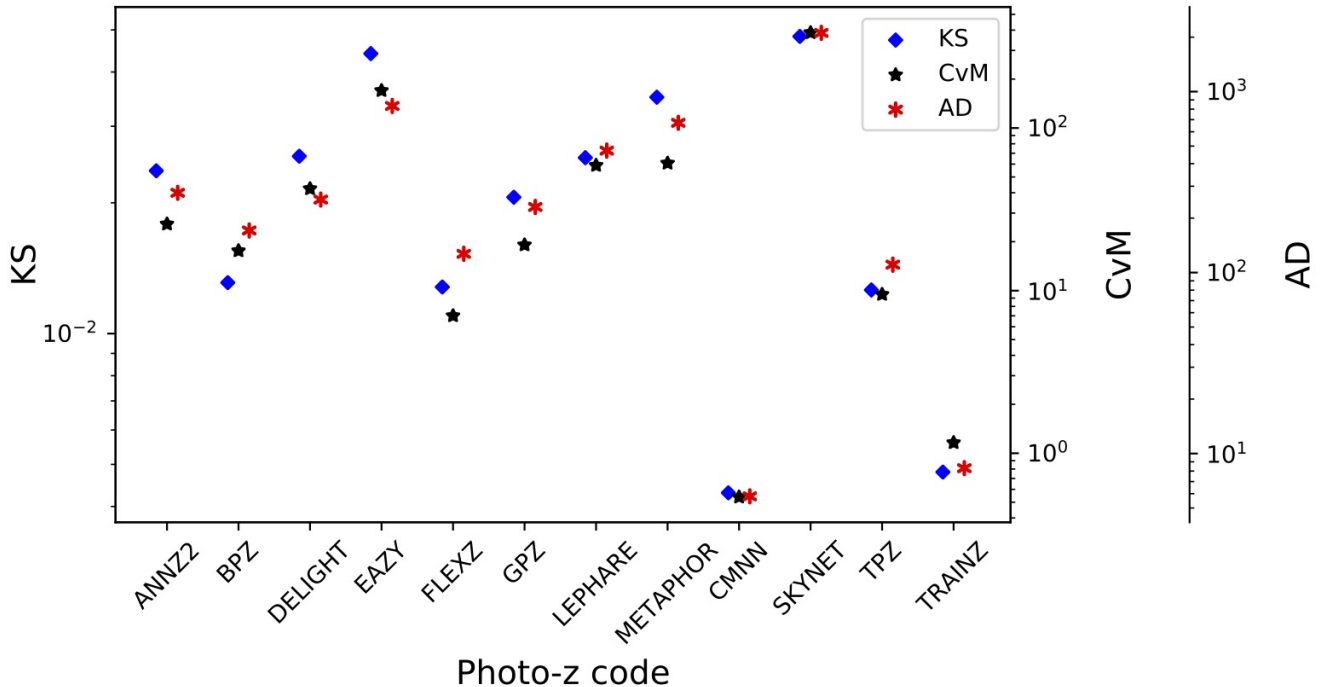


Figure 5. A visual representation of the Kolmogorov-Smirnov (KS, blue diamond), Cramer-von Mises (CvM, black star), and Anderson-Darling (AD, red asterisk) statistics for the $\hat{N}(z)$ distributions. The statistics are correlated, the codes with the lowest KS statistics tend to have the lowest CvM and AD statistics. CMNN performs markedly better than the others in reconstructing the overall $N(z)$ distribution, while SKYNET scores poorly due to an overall bias in its redshift predictions.

in the final $\hat{N}(z)$ estimate. TPZ performed quite poorly in ₁₃₀₉ $p(z)$ statistics, but results in a good fit to the overall $N(z)$. ₁₃₁₀ This is somewhat surprising, as performance was optimized ₁₃₁₁ for accurate $p(z)$, not $\hat{N}(z)$. During the validation stage for ₁₃₁₂ TPZ, there was a trade off between the width of the $p(z)$ ₁₃₁₃ when adjusting a smoothing parameter and overall redshift ₁₃₁₄ bias. The optimal result in the PIT metrics, as illustrated in ₁₃₁₅ the shape of the QQ plot, does contain some level of bias as ₁₃₁₆ well as a slight underprediction of mean $p(z)$ width, which ₁₃₁₇ translates to poor metric scores. This is something that will ₁₃₁₈ be looked into for TPZ in the future. ₁₃₁₉

It is also of note that all three template-based codes ₁₃₂₀ show an excess in their stacked $p(z)$ at $z \sim 1.3 - 1.4$. ₁₃₂₁ This redshift range corresponds to the wavelengths where ₁₃₂₂ the 4000 Angstrom break is passing between the borders of ₁₃₂₃ the z and y filters. This strong break entering the gap be- ₁₃₂₄ tween the two reddest filters can cause problems with red- ₁₃₂₅ shift estimation of individual galaxies, as can be seen in the ₁₃₂₆ point-estimate photo- z 's shown in Figure A1. This is not ₁₃₂₇ unique to this dataset, it is a common occurrence in photo- ₁₃₂₈ z estimation. The fact that similar excesses appear in Fig- ₁₃₂₉ ure 4 for ANN22 and METAPHOR shows that the effect is ₁₃₃₀ not limited to template-based codes. However, the lack of ₁₃₃₁ such a feature in the other codes shows that it is possible to ₁₃₃₂ eliminate the degeneracies. Further study on this issue may ₁₃₃₃ provide a solution for codes that suffer from this shortcom- ₁₃₃₄ ing. ₁₃₃₅

Table 3 shows the CDE loss statistic for each photo- z ₁₃₃₆ code. Once again FLEXZBOOST and CMNN score very well ₁₃₃₇ for the stacked $\hat{N}(z)$ metrics, as do GPZ and TPZ. The CDE ₁₃₃₈

loss measures how well individual PDFs are estimated, and codes with a low CDE loss tend to have good $\hat{N}(z)$ estimates (though the reverse is not necessarily true). FLEXZBOOST is optimized to minimize CDE loss which may explain why the method has good ensemble metrics as well. Note from Table 3 that both FLEXZBOOST and CMNN have low CDE losses. Empirically, we have found that PIT RMSE is not as closely correlated to CDE loss as it is to the $N(z)$ statistics. As CDE loss is a better measure of individual redshift performance, rather than ensemble distribution performance, this statistic is a better indicator of which codes will be most likely to perform well for science cases where single objects are employed.

Table 4 gives the root-mean-square-error (RMSE) statistics for both the PIT and $N(z)$ estimators. The PIT value calculates the RMSE between the quantiles shown in the QQ plot in Figure 2 and the diagonal, while the $N(z)$ calculates the RMSE between the cumulative distribution of the stacked $\hat{N}(z)$ and the true redshift distribution $N'(z)$.

Table 5 lists the first three moments of the stacked $\hat{N}(z)$ distribution, including the moments of the “truth” distribution for comparison. Several codes are able to reproduce the mean and variance of the distribution to less than a per cent, while several codes do not, which may be a cause for concern, given that mean and variance of the redshift distribution are key properties in cosmological analyses. We note that this stated goal of the study as defined for participants was to accurately reproduce $p(z)$, the “stacking” of the probability distributions to estimate $\hat{N}(z)$ was not the focus as stated to the participants. This explains why some of the

best-performing empirical codes in terms of $p(z)$ measures (e. g. FLEXZBOOST) do not do as well at reproducing $\hat{N}(z)$ moments. Had we defined a different parameter to optimize, in this case overall accuracy of $\hat{N}(z)$ rather than individual $p(z)$, would result in improved performance in a particular metric. That is, optimizing photo- z performance for one metric does not automatically give optimal performance for other metrics. As previously stated, there are a variety of scientific use cases for photo- z 's in large upcoming surveys, and care must be taken in how the metrics used to optimize catalog photometric redshifts are defined as well as in how they are used. In addition, very few scientific use cases will employ the overall $\hat{N}(z)$ with no cuts, as we explore in this paper. We discuss more realistic tomographic bin selections that will be explored in a follow-up paper in Section 6.1.

5.3 Interpretation of metrics

Samples from accurate photo- z posteriors should reproduce the space of $p(z, data)$. However, it is difficult to test this reconstruction given our data set, as the galaxy distributions arise from mock objects pasted on to an underlying dark matter halo catalogue with properties designed to match empirical relations, rather than being drawn from statistical distributions in redshift. In previous sections we have mentioned that optimizing for a specific metric does not guarantee good performance on other metrics, nor is there any guarantee that good performance by our metrics corresponds to *accurate* photo- z posteriors. In other words, we can construct photo- z estimators that provide good coverage in many of our tests, but which have very little predictive power.

The TRAINZ estimator, which assigns every galaxy a $p(z)$ equal to $N(z)$ of the training set as described in Section 3.3, is introduced as a “null test” to demonstrate this point via *reductio ad absurdum*. TRAINZ outperforms all codes on the PIT-based metrics, and all but one code on the $N(z)$ based statistics. Because our training set is perfectly representative of the test set, $N(z)$ should be identical for both sets down to statistical noise.

The CDE loss and point estimate metrics, however, successfully identify problems with TRAINZ. As shown in Appendix A, TRAINZ has identical $ZPEAK$ and $ZWEIGHT$ values for every galaxy, and thus the photo- zs are constant as a function of spec- zs , i.e. a horizontal line at the mode and mean of the training set distribution respectively. The explicit dependence on the *individual posteriors in the calculation of the CDE loss*, described in Section 4.1.3, distinguishes this metric from the other $p(z)$ metrics that test the overall ensemble of $p(z)$ distributions. With a representative training set, TRAINZ will score well on the ensemble metrics, but fails miserably for metrics tied to individual redshifts. We note that many of the ensemble-based metrics are prominent in the photo- z literature despite their inability to identify problems such as those exemplified by TRAINZ.

In summary, context is crucial to interpreting metrics and defending against the likes of TRAINZ. The best photo- z method is the one that most effectively achieves our science goals, not the one that performs best on a metric that does not accurately reflect those goals. In the absence of clear goals or the information necessary for a principled metric

Table 3. CDE loss statistic for each photo- z code.

Photo- z Code	CDE Loss
ANNZ2	-6.88
BPZ	-7.82
DELIGHT	-8.33
EAZY	-7.07
FLEXZBOOST	-10.60
GPz	-9.93
LEPHARE	-1.66
METAPHoR	-6.28
CMNN	-10.43
SKYNET	-7.89
TPZ	-9.55
TRAINZ	-0.83

Table 4. Root-Mean-Square-Error (RMSE) statistics for the eleven photo- z codes for both PIT and $\hat{N}(z)$ distributions.

Photo- z Code	PIT RMSE	$N(z)$ RMSE
ANNZ2	0.019	0.0054
BPZ	0.032	0.0050
DELIGHT	0.111	0.0056
EAZY	0.054	0.0102
FLEXZBOOST	0.021	0.0022
GPz	0.027	0.0042
LEPHARE	0.028	0.0062
METAPHoR	0.064	0.0081
CMNN	0.108	0.0009
SKYNET	0.054	0.0144
TPZ	0.082	0.0031
TRAINZ	0.0025	0.0013

definition, we must think carefully before choosing a single metric

6 DISCUSSION

In this paper we presented results evaluating the photometric redshift PDF computation for eleven photo- z codes. As discussed in Section 4 the $p(z)$ should accurately reflect the relative likelihood as a function of redshift for each galaxy. All codes were provided a set of representative training data and tested on an idealized set of model galaxies with high signal-to-noise and photometry with no confounding effects due to blending, instrumental effects, the night sky, etc... included. The goal was not to determine a “best” photo- z code: in many ways, this was a baseline test of a “best case scenario” to predict the expected photo- z performance if a stage IV dark energy survey was to obtain complete training samples and perfectly calibrated their multi-band photometry. Given these idealized conditions, any deficiencies observed in a photo- z code’s performance should be a cause for concern, and may be evidence in a problem with either/both of the specific code implementation or the underlying algorithm. In order to meet the stringent LSST requirements on photo- z performance, identifying and correcting such prob-

Table 5. Moments of the stacked $\hat{N}(z)$ distribution

Stacked $n(z)$ Moments			
	1st Moment	2nd Moment	3rd Moment
TRUTH	0.701	0.630	0.671
Photo-z Code	1st Moment	2nd Moment	3rd Moment
ANNz2	0.702	0.625	0.653
BPZ	0.699	0.629	0.671
DELIGHT	0.692	0.609	0.638
EAZY	0.681	0.595	0.619
FLEXZBOOST	0.694	0.610	0.631
GPz	0.696	0.615	0.639
LEPHARE	0.718	0.668	0.741
METAPHO.R	0.705	0.628	0.657
CMNN	0.701	0.628	0.667
SKYNET	0.743	0.708	0.797
TPZ	0.700	0.619	0.643
TRAINZ	0.699	0.627	0.666

lems is an important first step before tackling more realistic data in future challenges. Most of the codes tested performed well, however, several did not meet the stringent goals that have been laid out for LSST photometric redshift performance. This is a cause for concern, given the idealized conditions, and the individual code responses will be studied in detail moving forward. One obvious trend in several of the codes tested was an overall over or underprediction of the widths of $p(z)$, as evidenced by the QQ plots and PIT histograms shown in Fig. 2. A more careful tuning of bandwidth or smoothing during the validation process appears to be necessary for many of the machine learning based codes in order to improve the accuracy of $p(z)$. For narrow peaked $p(z)$ the parameterization of the PDF as evaluated on a fixed redshift grid could also have contributed to some overestimates of $p(z)$ width simply due to the finite resolution. After evaluating results such as those presented in Malz et al. (2018), in future analyses we plan to switch from a fixed grid to quantile-based storage of $p(z)$ in order to more efficiently and accurately store redshift PDF results.

Another important factor to keep in mind when examining the results presented in this paper is the fact that they are at some level dependent on the metrics that we aim to optimize: in this case code participants were asked to submit their optimal measures of an accurate $p(z)$, so participants used the training/validation data to optimize their codes accordingly. Had we, instead, asked for an optimal $\hat{N}(z)$ the resulting metrics would be different for most, if not all, of the codes, as they would optimize toward a different goal. Specific metric choice can affect which codes are among the “best” codes. As stated earlier, there are cosmological science cases that require either individual galaxy photo-z measures, or ensemble $\hat{N}(z)$ measures. We must be aware of that the optimal method for one is not necessarily optimal for the other, and in fact several photo-z algorithms may be necessary in the final cosmological analysis in order to satisfy the requirements of all science use cases. The example of the simple TRAINZ estimator described in Section 5.3 shows a simple model with a $p(z)$ that is unrealistic for individual objects can still score very well on many of our metrics. It is important to look at all metrics, and keep in mind what

information each metric conveys. We re-emphasize that the dataset tested was quite idealized, and discuss enhancements that will be added in future simulations to test photo-z codes on increasingly realistic conditions in the following section.

6.1 Future work

The work presented in this paper is only the first step in characterizing current photo-z codes and moving toward an improved photometric redshift estimator. This initial paper explored code performance in idealized conditions with perfect catalog-based photometry and representative training data. As mentioned in Section 5.2 for the stacked $N(z)$ metrics we examined only the entire galaxy population with no selections in either photo-z “quality” or redshift. The cosmological analyses for weak lensing and large scale structure based measures plan to break galaxy samples into tomographic redshift bins, using photo-z $p(z)$ to infer the redshift distribution for each bin. The specific selection used to determine these bins, both algorithmically and the specific bin boundaries, could induce biases due to indirect selections inherent in the photo-z or other bin selection parameters. The effects of tomographic bin selection will be explored in a dedicated future paper. [are there any references for this? I remember Gary Bernstein talking about this at a photo-z workshop in Japan, but I don’t know that it was published. I believe Michael Troxel has discussed this as well.] We also plan to propagate the uncertainties measured in a set of fiducial tomographic redshift bins in order to estimate impact on cosmological parameter estimation.

In future papers we will add more and more complexity to our simulated data in order to test photo-z algorithms in increasingly realistic conditions. The most pressing concern is the impact of incomplete spectroscopic training samples. As discussed extensively in Newman et al. (2015) a representative set of spectroscopically confirmed galaxies spanning the full range of both redshift and apparent magnitude is necessary as a training set to characterize the mapping from broad-band fluxes to photometric redshifts. However, due to a combination of factors due to both the galaxy SEDs and limitations of spectrographic instruments, redshift samples are known to be systematically incomplete, where certain galaxy types and redshift intervals fail to yield a redshift even at the longest integration times on current and near-future instruments. The more representative the training data, the better the performance of photo-z algorithms will be. Current and upcoming surveys are putting in significant effort into obtaining these training samples (e. g. Masters et al. 2017), however we still expect significant incompleteness for LSST-like samples, particularly at faint magnitudes. One major focus of an upcoming LSST Dark Energy Science Collaboration Photo-z Working Group data challenge is to produce a realistically incomplete training set of spectroscopic galaxies, modeling the performance of spectrographs, emission-line properties, and expected signal-to-noise to determine which galaxies will fail to yield a secure redshift. In addition to outright redshift failures we will model the inclusion of a small number of falsely identified secure redshifts where misidentified emission lines or noise spikes cause an incorrect redshift solution to be marked as a high quality identification. Even sub-per cent level contamination by false redshifts can impact photo-z solutions at levels comparable

to the stringent requirements of some LSST science cases. We expect different systematics to occur in different photo-z codes in response to training on incomplete data, particularly some of the machine learning methods. The response of the codes will inform future directions of code development.

This initial paper explored a data set that was constructed at the catalog level, with no inclusion of the complications that come from measuring photometry from images. Future data challenges will move to catalogs constructed from mock images, including effects that will have great impact on photo-z measurements. Object blending will be a major area of investigation, as the mixing of flux from multiple objects and the resultant change in measured colours is predicted to affect a large fraction of LSST galaxies (Dawson et al. 2016), and will be one of the major contributing systematics for photo-z's. Inclusion of differing observing conditions (seeing, clouds, variations in filter curves, Galactic dust, ...), as well as models for instrumental and system effects, sky masks, will all impact object photometry, and will be explored in the upcoming data challenge and their impacts described in upcoming papers. All underlying SEDs were parameterized as a weighted combination of five basis SEDs, with no additional accounting for host galaxy dust obscuration beyond what was encoded in the basis templates. This, in effect, limited the simulation to a very simple model of internal obscuration. Future simulations will include a more complicated and realistic treatment of host galaxy dust.

The underlying simulation used in this work was based on a light-cone constructed to a maximum redshift of $z = 2$. LSST imaging after 10 years of observations will include a significant number of $z > 2$ galaxies in expected cosmology samples, and their inclusion does have potential significant implications for photo-z measures: the high redshift galaxies lie at fainter apparent magnitudes and can have anomalous colours due to evolution of stellar populations and the shift to rest-frame magnitudes probing UV features of the underlying SED. More importantly, one of the most common “catastrophic outlier” degeneracies observed in deep photometric samples occurs when the Lyman break is mistaken for the Balmer break, leading to multiple redshift solutions at $z \sim 0.2 - 0.3$ and $z \sim 2 - 3$ (Massarotti et al. 2001). This degeneracy, along with other potential degeneracies, are currently not covered by the limited redshift range of this initial paper, which could mean that we are not probing the full range of potential extreme outlier populations and how our photo-z estimators respond to them. Extending simulations to include the high-redshift galaxy population will be a priority in future data challenges.

1521 to identify AGN dominated galaxies, but also obtain more accurate
 1522 photometric redshifts (e.g. Salvato et al. 2011).

In addition to AGN dominated galaxies, those with lower levels of nuclear activity present a more insidious problem, where AGN features may not be apparent, but the colors and other host galaxy properties are perturbed relative to galaxies with an inactive nucleus. In such cases, the presence of the AGN may induce a bias if the template SEDs or empirical datasets do not include low-level AGN counterparts. For LSST, we will need to identify and obtain accurate photometric redshifts of all types of AGN for a range of science goals, whether it is to eliminate such objects from cosmology experiments, or to use them with confidence, all the way through to understanding galaxy evolution and the role that AGN may play in influencing galaxy properties over cosmic time.

A promising route to classifying and obtaining accurate photometric redshifts for the AGN population is by combining machine learning with template-fitting techniques, as has recently been demonstrated by Duncan et al. (2018) for radio-selected AGN. This is because AGN are relatively easy to obtain spectroscopic redshifts for over all redshifts due to the strong emission lines that they exhibit, allowing very good training sets for machine learning algorithms to use. Whereas for those galaxies where the AGN is sub-dominant the galaxy templates are still adequate for obtaining reasonable photometric redshifts.

In addition to these improvements, the DESC Photo-z group plans to look at all potential methods to combine the results from multiple photo-z codes to improve $p(z)$ accuracy, similar to the work presented in Dahlen et al. (2013); Carrasco Kind & Brunner (2014); Duncan et al. (2018). Taking advantage of multiple algorithms that use observables in slightly different ways has shown promise, however we must be very conscious of whether a potential combination properly treats the covariance between the methods, given that they are estimating quantities based on the same underlying observables. Several science cases wish to estimate physical quantities along with redshift, for example galaxy stellar mass and star formation rate. Proper joint estimation of redshift and physical quantities requires an in depth understanding of galaxy evolution, and progress on accurate bivariate redshift probability distributions will go hand in hand with progress on understanding galaxies themselves. Parameterization and storage of a complex 2-dimensional probability surface for potentially billions of galaxies (or even subsets of hundreds of thousands of particular interest) pose a potential challenge. These issues will be examined in another future paper.

Finally, while this paper and future papers discussed above focus on photometric redshift codes and estimating accurate $p(z)$ from training data, we plan a separate, but complementary, project to examine calibration of the resultant redshifts via spatial cross-correlations (Newman 2008), which will be explored in a separate series of future papers. The overarching plan describing everything laid out in this section is described in more detail in the LSST DESC Science Roadmap (see Footnote in Section 1). These plans will require significant effort, but they are necessary if we are to make optimal use of the LSST data for astrophysical and cosmological analyses.

1569 7 CONCLUSION

1570 In this study we have not accounted for the presence of Active Galactic Nuclei (AGN) contributions to galaxy fluxes.
 1571 In some cases, AGN will be easily identified from the colors and morphologies, i.e. the case of the brightest quasars where the nuclear activity outshines the host galaxy, and numerous studies have utilized color selection to create large samples of quasars (e.g. Richards et al. 2006; Maddox et al. 2008; Richards et al. 2015). In current deep fields, similar in depth to what we expect from LSST, variability information and multi-wavelength data have been critical to not only iden-

1641 **Acknowledgments**

1642 Author contributions are listed below.
 1643 *S.J. Schmidt:* Led the project. (conceptualization, data 1705
 1644 curation, formal analysis, investigation, methodology, 1706
 1645 project administration, resources, software, supervision, 1707
 1646 visualization, writing – original draft, writing – review & 1708
 1647 editing)
 1648 *A.I. Malz:* Contributed to choice of metrics, implementation 1710
 1649 in code, and writing. (conceptualization, methodology, 1711
 1650 project administration, resources, software, visualization, 1712
 1651 writing – original draft, writing – review & editing) 1713
 1652 *J.Y.H. Soo:* Ran ANNz2 and Delight, updated abstract, 1714
 1653 edited sections 1 through 6, added tables in Methods 1715
 1654 and Results, updated references.bib and added references 1716
 1655 throughout the paper 1717
 1656 *M. Brescia:* main ideator of METAPHOR and of MLPQNA; 1718
 1657 modification of METAPHOR pipeline to fit the LSST data 1719
 1658 structure and requirements 1720
 1659 *S. Cavuoti:* Contributed to choice and test of metrics, ran 1721
 1660 METAPHOR, minor text editing 1722
 1661 *G. Longo:* Scientific advise, test and validation of the 1723
 1662 modified METAPHOR pipeline, text of the METAPHOR 1724
 1663 section
 1664 *I.A. Almosallam:* vetted the early versions of the data set
 1665 and ran many photo-z codes on it, applied GPz to the final 1725
 1666 version and wrote the GPz subsection
 1667 *M.L. Graham:* Ran the colour-matched nearest-neighbours 1726
 1668 photo-z code on the Buzzard catalog and wrote the relevant 1727
 1669 piece of Section 2; participated in discussions of the analy- 1728
 1670 sis.
 1671 *A.J. Connolly:* Developed the colour-matched nearest- 1730
 1672 neighbours photo-z code; participated in discussions of the 1731
 1673 analysis.
 1674 *E. Nourbakhsh:* Ran and optimized TPZ code on the 1733
 1675 Buzzard catalog and wrote a subsection of Section 2 for that 1734
 1676 *J. Cohen-Tanugi:* contributed to running code, analysis 1735
 1677 discussion, and editing, reviewing the paper 1736
 1678 *H. Tranin:* contributed to providing SkyNet results and 1737
 1679 writing the relevant section 1738
 1680 *P.E. Freeman:* Contributed to choice of CDE metrics and 1739
 1681 to implementation of FlexZBoost 1740
 1682 *K. Iyer:* assisted in writing metric functions used to evaluate 1741
 1683 codes 1742
 1684 *J.B. Kalmbach:* Worked on preparing the figures for the 1743
 1685 paper. 1744
 1686 *E. Kovacs:* Ran simulations, discussed data format and 1745
 1687 properties for SEDs, dust, and ELG corrections 1746
 1688 *A.B. Lee:* Co-developed FlexZBoost and the CDE loss statis- 1747
 1689 tic, wrote text on the work, and supervised the development 1748
 1690 of FlexZBoost software packages 1749
 1691 *C. Morrison:* Managerial support; Discussions with authors 1750
 1692 regarding metrics and style; Some coding contribution to 1751
 1693 metric computation. 1752
 1694 *J. Newman:* Contributions to overall strategy, design of 1753
 1695 metrics, and supervision of work done by Rongpu Zhou 1754
 1696 *E. Nuss:* contributed to running code, analysis discussion, 1755
 1697 and editing, reviewing the paper 1756
 1698 *T. Pospisil:* Co-developed FlexZBoost software and CDE 1757
 1699 loss calculation code 1758
 1700 *M.J. Jarvis:* Contributed text on AGN to Discussion section 1759
 1701 and portions of GPz work 1760

1702 *R. Izbicki:* Co-developed FlexZBoost and the CDE loss
 1703 statistic, and wrote software for FlexZBoost

The authors would like to thank their LSST-DESC publication review committee.

AIM is advised by David W. Hogg and was supported by National Science Foundation grant AST-1517237.

The DESC acknowledges ongoing support from the Institut National de Physique Nucléaire et de Physique des Particules in France; the Science & Technology Facilities Council in the United Kingdom; and the Department of Energy, the National Science Foundation, and the LSST Corporation in the United States. DESC uses resources of the IN2P3 Computing Center (CC-IN2P3-Lyon/Villeurbanne - France) funded by the Centre National de la Recherche Scientifique; the National Energy Research Scientific Computing Center, a DOE Office of Science User Facility supported by the Office of Science of the U.S. Department of Energy under Contract No. DE-AC02-05CH11231; STFC DiRAC HPC Facilities, funded by UK BIS National E-infrastructure capital grants; and the UK particle physics grid, supported by the GridPP Collaboration. This work was performed in part under DOE Contract DE-AC02-76SF00515.

APPENDIX A: POINT ESTIMATE PHOTOMETRIC REDSHIFTS

While we do not recommend the use of single point estimates of redshift for most science applications, plots of the point estimates can be a useful qualitative diagnostic of photo-z code performance, i. e. examining point photo-z vs. spec-z plots visually can give a quick impression of some common trends in different codes. Computing point estimate statistics may also be useful for more direct comparisons with previous photo-z evaluations. If a point-estimate is preferred for a specific science case, it is fairly simple to compute the mean, mode, or some other simple estimator from each $p(z)$, so these point estimates can be easily derived from the stored $p(z)$.

There are several common point estimators of photo-z posteriors employed by different codes, e. g. the mode, mean, median of the $p(z)$ distribution. In addition, many of the machine learning based estimators can be set up to return a single redshift solution. For example, SkyNet can be configured to run as a regressor that returns a single float rather than a classifier that returns a 200-bin $p(z)$ estimate. The single value returned by a machine learning based code may not correspond to a particular measure such as the mode or mean, and so to avoid interpretation of results that might be introduced by variations in choice of specific point-estimate implementation per code, we discard the code-specific point estimates. We instead calculate point estimates more uniformly across the codes directly from the $p(z)$ using two measures, z_{PEAK} and z_{WEIGHT} . z_{PEAK} is simply the maximum value attained for each galaxy $p(z)$, the mode of the probability distribution. z_{WEIGHT} is defined similarly to how it is defined in Dahlen et al. (2013), as the weighted mean of the redshift over the main peak of $p(z)$ containing the z_{PEAK} value. The main peak is defined by subtracting $0.05 \times z_{\text{PEAK}}$ from $p(z)$ and identifying the roots to isolate the peak containing z_{PEAK} , z_{WEIGHT} is defined as the weighted mean

redshift within this peak. We restrict to a single peak in order to avoid confusion from bimodal and multimodal $p(z)$ such as those shown in bottom panels of Figure 1. For example, for a bimodal probability distribution a weighted mean calculated over both peaks would fall between the peaks, at a redshift where the probability is minimal. Restricting the weighting to a single peak ensures that the point estimate will fall in the region of maximum redshift probability.

A1 Point Estimate Metrics

We calculate the commonly used point estimate metrics of the overall photo-z scatter (σ_z , the standard deviation of the photo-z residuals), bias, and “catastrophic outlier rate”. Specifically, we calculate the metrics as follows: we define e_z as

$$e_z = \frac{z_p - z_s}{1 + z_s} \quad (\text{A1})$$

where z_p is the point estimate and z_s is the true redshift. In practice, because the standard deviation calculation is quite sensitive to the outliers, we define the photo-z scatter, σ in terms of the Interquartile Range (IQR), the difference between the 75th and 25th percentiles of the e_z distribution. In order to match the usual meaning of a 1σ interval, we scale the IQR and define $\sigma_{IQR} = IQR/1.349$, as there is a factor of 1.349 difference between the IQR and the standard deviation of a Normal distribution. While many other studies define the bias based on the mean offset between true and estimated redshift, in this study we define the bias as the median value of e_z for the sample. We use median as it is, once again, less sensitive to outliers than the mean. The catastrophic outlier fraction is defined as the fraction of galaxies with e_z greater than the larger of $3\sigma_{IQR}$ or 0.06, i.e. 3σ outliers with a floor of $\sigma_{IQR}=0.02$. For reference, the goals stated in Section 3.8 of the LSST Science Book (Abell et al. 2009) for photo-z performance in these metrics, assuming perfect training knowledge (as we are testing in this paper) are:

- RMS scatter < $0.02(1+z)$
- bias < 0.003
- catastrophic outlier rate < 10%

These definitions are similar, but not exactly the same, as the σ_{IQR} and median bias calculated here, but are similar enough for qualitative comparisons to the LSST goals.

Fig. A1 shows the point estimates for both z_{PEAK} and z_{WEIGHT} . Point density is shown with mixed contours to emphasize that most of the galaxies do fall close to the $z_{phot} = z_{spec}$ line, while blue points show differing characteristics of the outlier populations. The red dashed lines indicated the cutoff for catastrophic outliers, defined as: $\max(0.06, 3\sigma_{IQR})$. As with the full $p(z)$ results, a variety of behaviours are evident in the different codes. Table A1 lists the scatter, bias, and catastrophic outlier fractions for the codes. The performance of the codes for point metrics is highly correlated with performance on $p(z)$ based tests, which is to be expected, given that the point-estimates were derived from the $p(z)$. Some discretization is evident in z_{PEAK} , particularly for SKYNET, due to the finite grid spacing of the reported $p(z)$. These discreteness effects are mitigated by the

weighting of z_{WEIGHT} , resulting in a smoother distribution of redshift estimates. Several features perpendicular to the main $z_{phot} = z_{spec}$ line are evident. These features are due to the 4000 angstrom break passing through the gaps between adjacent LSST filters. These features are most prominent in template-based codes, but appear to some degree in all codes tested.

In even the best performing codes, there are visible occupied regions away from the $z_{phot} = z_{spec}$ line, corresponding to degenerate redshift solutions for certain LSST magnitudes and colors. While use of the full information available via $p(z)$ mitigates their impact, a full understanding of the outlier population is critical for LSST science, particularly in tomographic applications

Finally, we note that all eleven codes are at or near the goals for point-estimates as outlined in the LSST Science Requirements Document¹⁹ and Graham et al. (2018). This is to be expected, given that the requirements were designed such that a point estimate photo-z would meet these requirements for perfect training data to a depth of $i < 25$. But, it is still an encouraging sign, given an updated mock galaxy simulation and the expanded set of photo-z codes tested.

REFERENCES

- Abbott T., et al., 2005, preprint (arXiv:astro-ph/0510346)
 Abell P. A., et al., 2009, preprint (arXiv:0912.0201),
 Athara H., et al., 2018a, *PASJ*, **70**, S4
 Athara H., et al., 2018b, *PASJ*, **70**, S8
 Almosallam I. A., Lindsay S. N., Jarvis M. J., Roberts S. J., 2016a, *MNRAS*, **455**, 2387
 Almosallam I. A., Jarvis M. J., Roberts S. J., 2016b, *MNRAS*, **462**, 726
 Arnouts S., Cristiani S., Moscardini L., Matarrese S., Lucchin F., Fontana A., Giallongo E., 1999, *MNRAS*, **310**, 540
 Behroozi P. S., Wechsler R. H., Wu H.-Y., 2013, *ApJ*, **762**, 109
 Benítez N., 2000, *ApJ*, **536**, 571
 Biviano A., et al., 2013, *A&A*, **558**, A1
 Blanton M. R., Roweis S., 2007, *AJ*, **133**, 734
 Blanton M. R., et al., 2005, *AJ*, **129**, 2562
 Bonnett C., 2015, *MNRAS*, **449**, 1043
 Bonnett C., et al., 2016, *Phys. Rev. D*, **94**, 042005
 Brammer G. B., van Dokkum P. G., Coppi P., 2008, *ApJ*, **686**, 1503
 Breiman L., Friedman J. H., Olshen R. A., Stone C. J., 1984, *Classification and Regression Trees, Statistics/Probability Series*. Wadsworth Publishing Company, Belmont, California, U.S.A
 Brescia M., Cavaudi S., D'Abrusco R., Longo G., Mercurio A., 2013, *ApJ*, 772
 Brescia M., Cavaudi S., Longo G., De Stefano V., 2014, *A&A*, 568
 Brescia M., Cavaudi S., Amaro V., Riccio G., Angora G., Vellucci C., Longo G., 2018, preprint, (arXiv:1802.07683)
 Carrasco Kind M., Brunner R. J., 2013, *MNRAS*, **432**, 1483
 Carrasco Kind M., Brunner R. J., 2014, *MNRAS*, **442**, 3380
 Cavaudi S., Brescia M., De Stefano V., Longo G., 2015, *Exp. Astron.*, **39**, 45
 Cavaudi S., Amaro V., Brescia M., Vellucci C., Tortora C., Longo G., 2017a, *MNRAS*, **465**, 1959
 Cavaudi S., et al., 2017b, *MNRAS*, **466**, 2039

¹⁹ available at: <http://ls.st/srd>

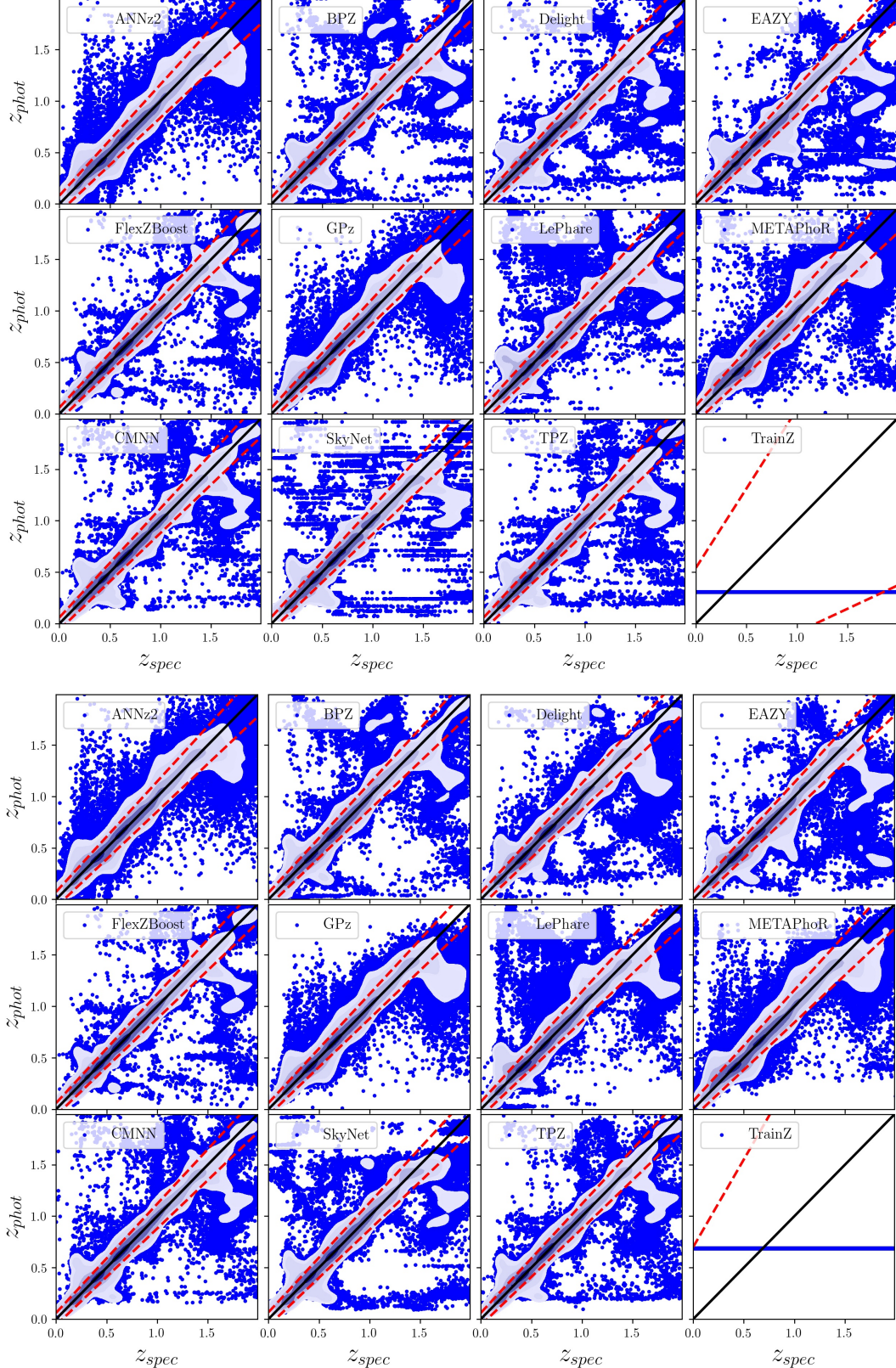


Figure A1. Point estimate photo-z's derived from the posteriors. Top panel shows z_{PEAK} , while bottom panel shows z_{WEIGHT} . Point estimate density is represented with fixed density contours, while outliers at lower density are represented by blue points. While use of point-estimate photo-z's is not recommended, they do make for useful comparative and visual diagnostics. In the lower-right panel of each plot, the TRAINZ estimator results in identical photo-z estimates at the mode and mean of the training set $N'(z)$ distribution for all galaxies.

Table A1. Point estimate statistics

Photo-z Code	ZPEAK			ZW EIGHT		
	$\frac{\sigma_{IQR}}{(1+z)}$	median	outlier fraction	$\frac{\sigma_{IQR}}{(1+z)}$	median	outlier fraction
ANNz2	0.0270	0.00063	0.044	0.0244	0.000307	0.047
BPZ	0.0215	-0.00175	0.035	0.0215	-0.002005	0.032
DELIGHT	0.0212	-0.00185	0.038	0.0216	-0.002158	0.038
EAZY	0.0225	-0.00218	0.034	0.0226	-0.003765	0.029
FLEXZBOOST	0.0154	-0.00027	0.020	0.0148	-0.000211	0.017
GPz	0.0197	-0.00000	0.052	0.0195	0.000113	0.051
LEPHARE	0.0236	-0.00161	0.058	0.0239	-0.002007	0.056
METAPHOR	0.0264	0.00000	0.037	0.0262	0.001333	0.048
CMNN	0.0184	-0.00132	0.035	0.0170	-0.001049	0.034
SKYNET	0.0219	-0.00167	0.036	0.0218	0.000174	0.037
TPZ	0.0161	0.00309	0.033	0.0166	0.003048	0.031
TRAINZ	0.1808	-0.2086	0.000	0.2335	0.022135	0.000

- 1876 Chen T., Guestrin C., 2016, in *Proceedings of the 22Nd ACM 1922
1877 SIGKDD International Conference on Knowledge Discovery 1923
1878 and Data Mining. KDD '16. ACM, New York, NY, USA, pp 1924
1879 785–794, doi:10.1145/2939672.2939785, <http://doi.acm.org/10.1145/2939672.2939785>*
- 1880 Dahlen T., et al., 2013, *ApJ*, **775**, 93
- 1881 Dawson W. A., Schneider M. D., Tyson J. A., Jee M. J., 2016, *ApJ*, **816**, 11
- 1882 Duncan K. J., Jarvis M. J., Brown M. J. I., Röttgering H. J. A., 2018, *Monthly Notices of the Royal Astronomical Society*, **479**, p. 940
- 1883 Fernández-Soto A., Lanzetta K. M., Yahil A., 1999, *ApJ*, **513**, 34
- 1884 Firth A. E., Lahav O., Somerville R. S., 2003, *MNRAS*, **339**, 1195
- 1885 Freeman P. E., Izbicki R., Lee A. B., 2017, *MNRAS*, **468**, 4556
- 1886 Graff P., Feroz F., Hobson M. P., Lasenby A., 2014, *MNRAS*, **441**, 1741
- 1887 Graham M. L., Connolly A. J., Ivezic Ž., Schmidt S. J., Jones R. L., Jurić M., Daniel S. F., Yoachim P., 2018, *AJ*, **155**, 1
- 1888 Green J., et al., 2012, preprint (arXiv:1208.4012),
- 1889 Hildebrandt H., et al., 2010, *A&A*, **523**, A31
- 1890 Hofmann B., Mathé P., 2018, *Inverse Problems*, **34**, 015007
- 1891 Ibert O., et al., 2006, *A&A*, **457**, 841
- 1892 Ivezic Ž., et al., 2008, preprint (arXiv:0805.2366),
- 1893 Izbicki R., Lee A. B., 2017, *Electron. J. Statist.*, **11**, 2800
- 1894 Izbicki R., Lee A. B., Freeman P. E., 2017, *Ann. Appl. Stat.*, **11**, 698
- 1895 Laigle C., et al., 2016, *ApJS*, **224**, 24
- 1896 Laureijs R., et al., 2011, preprint (1110.3193),
- 1897 Leistedt B., Hogg D. W., 2017, *ApJ*, **838**, 5
- 1898 Maddox N., Hewett P. C., Warren S. J., Croom S. M., 2008, *MNRAS*, **386**, 1605
- 1899 Malz A., Hogg D., in prep., CHIPPR, chippr
- 1900 Malz A., Marshall P., DeRose J., Graham M., Schmidt S., Wechsler R., 2018, *AJ*, Accepted,
- 1901 Mandelbaum R., et al., 2008, *MNRAS*, **386**, 781
- 1902 Massarotti M., Iovino A., Buzzoni A., 2001, *A&A*, **368**, 74
- 1903 Masters D. C., Stern D. K., Cohen J. G., Capak P. L., Rhodes J. D., Castander F. J., Paltani S., 2017, *ApJ*, **841**, 111
- 1904 Newman J. A., 2008, *ApJ*, **684**, 88
- 1905 Newman J. A., et al., 2015, *Astroparticle Physics*, **63**, 81
- 1906 Polsterer K. L., D'Isanto A., Gieseke F., 2016, preprint (arXiv:1608.08016),
- 1907 Rasmussen C., Williams C., 2006, *Gaussian Processes for Machine Learning. Adaptative computation and machine learn-*ing series, MIT Press, Cambridge, MA
- 1908 Rau M. M., Seitz S., Brimioulle F., Frank E., Friedrich O., Gruen D., Hoyle B., 2015, *MNRAS*, **452**, 3710
- 1909 Reddick R. M., Wechsler R. H., Tinker J. L., Behroozi P. S., 2013, *ApJ*, **771**, 30
- 1910 Riccio G., Brescia M., Cavuoti S., Mercurio A., di Giorgio A., Molinari S., 2017, *PASP*, **129**
- 1911 Richards G. T., et al., 2006, *ApJS*, **166**, 470
- 1912 Richards G. T., et al., 2015, *ApJS*, **219**, 39
- 1913 Sadeh I., Abdalla F. B., Lahav O., 2016, *PASP*, **128**, 104502
- 1914 Salvato M., et al., 2011, *ApJ*, **742**, 61
- 1915 Sánchez C., Bernstein G. M., 2018, preprint, (arXiv:1807.11873)
- 1916 Sánchez C., et al., 2014, *MNRAS*, **445**, 1482
- 1917 Scott D. W., 1992, *Multivariate Density Estimation. Theory, Practice, and Visualization*. Wiley
- 1918 Skrutskie M. F., et al., 2006, *AJ*, **131**, 1163
- 1919 Tanaka M., et al., 2017, preprint (arXiv:1704.05988),
- 1920 The LSST Dark Energy Science Collaboration et al., 2018, preprint, (arXiv:1809.01669)
- 1921 York D. G., et al., 2000, *AJ*, **120**, 1579
- de Jong J. T. A., Verdoes Kleijn G. A., Kuijken K. H., Valentijn E. A., 2013, *Exp. Astron.*, **35**, 25
- de Jong J. T. A., et al., 2017, *A&A*, **604**, A134